The Beijing Climate Center Climate System Model (BCC-CSM): Main Progress from CMIP5 to CMIP6

Tongwen Wu[1*], Yixiong Lu[1], Yongjie Fang[1], Xiaoge Xin[1], Laurent Li[1,2], Weiping Li[1], Weihua Jie[1], Jie Zhang[1], Yiming Liu[1], Li Zhang[1], Fang Zhang[1], Yanwu Zhang[1], Fanghua Wu[1], Jianglong Li[1], Min Chu[1], Zaizhi Wang[1], Xueli Shi[1], Xiangwen Liu[1], Min Wei[3], Anning Huang[4], Yaocun Zhang[4], Xiaohong Liu[1,5]

[1]Beijing Climate Center, China Meteorological Administration, Beijing, China

[2]Laboratoire de Météorologie Dynamique, IPSL, CNRS, Sorbonne Université, Ecole Normale Supérieure, Ecole Polytechnique, Paris, France

[3]National Meteorological Information Center, China Meteorological Administration, Beijing, China

[4]Nanjing University, Nanjing, China

[5]University of Wyoming, Laramie, WY, United States

Correspondence to: Tongwen Wu (twwu@cma.gov.cn)

(Revised on Feb. 10, 2019)

Abstract. Main progresses of Beijing Climate Center (BCC) climate system model from the phase five of the Coupled Model Intercomparison Project (CMIP5) to its phase six (CMIP6) are presented, in terms of physical parameterizations and model's performance. BCC-CSM1.1 and BCC-CSM1.1m are the two models involved in CMIP5. BCC-CSM2-MR, BCC-CSM2-HR, and BCC-ESM1.0 are the three models configured for CMIP6. Historical simulations from 1851 to 2014 from BCC-CSM2-MR (CMIP6) and from 1851 to 2005 from BCC-CSM1.1m (CMIP5) are used for models assessment. The evaluation matrices include (a) energy budget at top of the atmosphere, (b) surface air temperature, precipitation, and atmospheric circulation for global and East Asia regions, (c) sea surface temperature

(SST) in tropical Pacific, (d) sea ice extent and thickness and Atlantic Meridional Overturning Circulation (AMOC), and (e) climate variations at different time scales such as global warming trend in the 20th century, stratospheric quasi-biennial oscillation (QBO), Madden-Julian Oscillation (MJO) and diurnal cycle of precipitation. Compared to BCC-CSM1.1m, BCC-CSM2-MR shows significant improvements in many aspects including: tropospheric air temperature and circulation at global and regional scale in East Asia, climate variability at different time scales such as QBO, MJO, diurnal cycle of precipitation, interannual variations of SST in the equatorial Pacific, and long-term trend of surface air temperature.

1. Introduction

Changes of global climate and environment are main challenges that human societies are facing for sustainable developments. Climate and environment changes are often the consequence of combined effects of anthropogenic influences and complex interactions among the atmosphere, hydrosphere, lithosphere, cryosphere and biosphere of the Earth system. To better understand behaviors of the earth climate, and to predict its future evolution, appropriate new concepts and relevant methodologies should be proposed and developed. Climate system models are effective tools to simulate the interactions and feedbacks in an objective manner, and to explore their impacts on climate and climate change. The Coupled Model Intercomparison Project (CMIP) organized under the auspices of the World Climate Research Programme's (WCRP) Working Group on Coupled Modelling (WGCM) started twenty years ago as a comparison of a handful of early global coupled climate models (Meehl et al., 1997). More than 30 models participated in the phase five of CMIP (CMIP5, Taylor et al., 2012) and created an unprecedented dynamics in the scientific community to generate climate information and make them available for scientific researches. Many of these models were then extended into Earth System models by including the representation of biogeochemical cycles. BCC effectively contributed to CMIP5 by running most of the mandatory and optional simulations.

The first generation of Beijing Climate Center ocean-atmosphere Coupled Model BCC-CM1.0 was developed from 1995 to 2004 (e.g. Ding et al., 2002). It was mainly used for seasonal climate prediction. Since 2005, BCC initiated the development of a new fully-coupled climate modelling platform (Wu et

al., 2010, 2013, 2014). In 2012, two versions of the BCC model were released: BCC-CSM1.1 with a coarse horizontal resolution T42 (approximately 280 km) and BCC-CSM1.1m with a medium horizontal resolution T106 (approximately 110 km). It was a fully-coupled model with ocean, land surface, atmosphere, and sea-ice components (Wu et al., 2008; Wu, 2012; Xin et al., 2013). Both versions were extensively used for CMIP5. At the end of 2017, the second generation of the BCC model was released to run different simulations proposed by the phase six of CMIP (CMIP6, Eyring et al., 2016). The purpose of this paper is to document the main efforts and progress achieved in BCC for its climate model transition from CMIP5 to CMIP6. We show improvements in both model resolution and its physics. A relevant description on model transition, and experiment design are shown in Sections 2 and 3. A comparison of models performance is presented in Section 4. Conclusions and discussion are summaried in Section 5. Information about code and data availability is shown in Section 6.

2. Transition of the BCC climate system model from CMIP5 to CMIP6

Table 1 shows a summary of different BCC models or versions used for CMIP5 and CMIP6. All of them are fully-coupled global climate models with four components, atmosphere, ocean, land surface and sea-ice, interacting with each other. They are physically coupled through fluxes of momentum, energy, water at their interfaces. The coupling was realized with the flux coupler version 5 developed by the National Center for Atmosphere Research (NCAR). BCC-CSM1.1 and BCC-CSM1.1m are our two models involved in CMIP5. They differ only by their horizontal resolutions. As shown in Table 1, BCC-CSM2-MR, BCC-CSM2-HR, and BCC-ESM1.0 are the three models developed for CMIP6.

BCC-ESM1.0 is our Earth System configuration. It is a global fully-coupled climate-chemistry-carbon model, and intended to conduct simulations for the Aerosol Chemistry Model Intercomparison Project (AerChemMIP, Collins et al., 2017) and the Coupled Climate–Carbon Cycle Model Intercomparison Project (C4MIP, Jones et al., 2016), both endorsed by CMIP6. Its performance will be presented in a separated paper. BCC-CSM2-HR is our high-resolution configuration prepared for conducting simulations of the High Resolution Model Intercomparison Project (HighResMIP v1.0, Haarsma et al., 2016). It has 56 layers in the vertical, 0.092 hPa for the top of model. Its performance will also be presented separately.

In this paper, we focus on BCC-CSM1.1m and BCC-CSM2-MR. The two models are representative of our climate modelling efforts in CMIP5 and CMIP6 respectively. They have the same horizontal resolution (T106, about 110×110 km in the atmosphere and 30×30 km in the tropical ocean), ensuring a fair comparison. But they have different vertical resolutions in the atmosphere (Table 1), which are 26 layers with its top at 2.917 hPa in BCC-CSM1.1m and 46 layers with its top at 1.459 hPa in BCC-CSM2-MR (Figure 1). The present version of BCC-CSM2-MR takes 50% more computing time than BCC-CSM1.1m for the same amount of parallel computing processors.

2.1 Atmospheric component BCC-AGCM

The atmospheric component of BCC-CSM1.1m is BCC-AGCM2.2 (second generation). It is detailed in a series of publications (Wu et al., 2008, 2010; Wu, 2012; Wu et al., 2013). BCC-AGCM3-MR is its updated version (third generation), used as the atmosphere component in BCC-CSM2-MR. The dynamic core in the two models is identical and uses the spectral framework described in Wu et al. (2008), in which a reference stratified atmospheric temperature and a reference surface pressure are introduced into the governing equations to improve pressure gradient force and gradients of surface pressure and temperature, the prognostic variables for temperature and surface pressure are separately replaced by their perturbations from their references. Explicit time difference scheme is applied to vorticity equation, and semi-implicit time difference scheme for divergence, temperature, and surface pressure equations. Semi-Lagrangian tracer transport scheme is used for water vapor, liquid cloud water and ice cloud water. Main differences of model physics used in the two models (BCC-AGCM2.2 and BCC-AGCM3-MR) are summarized in Table 2 and details in the following:

a. Deep convection

Our second-generation atmospheric model, BCC-AGCM2.2, operates with a parameterization scheme of deep cumulus convection developed by Wu (2012). Main characteristics can be summarized as follows:

(1) Deep convection is initiated at the level of maximum moist static energy above the boundary layer. It is triggered when there is positive convective available potential energy (CAPE) and if the relative humidity of the air at the lifting level of convective cloud is greater than 75%;

(2) A bulk cloud model taking into account processes of entrainment/detrainment is used to calculate the convective updraft with consideration of budgets for mass, dry static energy, moisture, cloud liquid water, and momentum. The scheme also considers the lateral entrainment of the environmental air into the unstable ascending parcel before it rises to the lifting condensation level. The entrainment/detrainment amount for the updraft cloud parcel is determined according to the increase/decrease of updraft parcel mass with altitude. Based on a total energy conservation equation of the whole adiabatic system involving the updraft cloud parcel and the environment, the mass change for the adiabatic ascent of the cloud parcel with altitude is derived;

(3) The convective downdraft is assumed to be saturated and originated from the level of minimum environmental saturated equivalent potential temperature within the updraft cloud;

(4) The closure scheme determining the mass flux at the base of convective cloud is that suggested by Zhang (2002). It assumes that the increase/decrease of CAPE due to changes of the thermodynamic states in the free troposphere resulting from convection approximately balances the decrease/increase resulting from large-scale processes.

A modified version of Wu (2012) is used in BCC-AGCM3-MR for deep convection parameterization. The convection is triggered only when the boundary layer is unstable or there exists updraft velocity in the environment at the lifting level of convective cloud, and simultaneously there is positive CAPE. This modification is aimed to connect the deep convection to the instability of the boundary layer. The lifting condensation level is set to above the nominal level of non-divergence (600 hPa) in BCC-AGCM2.2 and lowered to the level of 650 hPa in BCC-AGCM3-MR. These modifications in the deep convection scheme are found to improve the simulation of diurnal cycle of precipitation and Madden-Julian Oscillation (MJO).

b. Shallow convection

Shallow convection is parameterized with a local convective transport scheme (Hack, 1994). It is used to remove any local instability that may remain after the deep convection scheme. This Hack convection scheme is largely-used one to typically represent shallow subtropical convection and midlevel convection that do not originate from the boundary layer.

c. Cloud macrophysics

Cloud macrophysics comprises physical processes to compute cloud fractions in each layer, horizontal and vertical overlapping of clouds, and conversion rates of water vapor into cloud condensates. In BCC-AGCM2.2, cloud fraction and the associated cloud macrophysics follow what designed in NCAR Community Atmosphere Model version 3 (CAM3, Collins et al., 2004). The total cloud cover (C_{tot}) within each model grid is set as the maximum value of three cloud covers: low-level marine stratus (C_{mst}), convective cloud (C_{conv}), and stratus cloud (C_s),

$$C_{tot} = \max\left(C_{conv}, C_{mst}, C_s\right) \tag{1}$$

As in CAM3, the marine stratocumulus cloud is diagnosed with an empirical relationship between the cloud fraction and the boundary layer stratification which is evaluated with atmospheric variables at surface and 700mb (Klein and Hartmann, 1993). The convective cloud fraction uses a functional form of Xu and Krueger (1991) relating the cloud cover to updraft mass flux from the deep and shallow convection schemes. The stratus cloud fraction is diagnosed on the basis of relative humidity which varies with pressure.

A new cloud scheme is developed and used in BCC-AGCM3-MR. It consists of calculating convective cloud and the total cloud cover in a different way from BCC-AGCM2.2. The total cloud fraction in each model grid cell is given as

$$C_{tot} = C_{conv} + \left(1 - C_{conv}\right)\max\left(C_{mst}, C_s\right) \tag{2}$$

And the convective cloud $\mathrm{C_{conv}}$ is assumed to be the sum of shallow ($C_{shallow}$) and deep (C_{deep}) convective cloud fractions:

$$C_{conv} = C_{shallow} + C_{deep} \tag{3}$$

$C_{shallow}$ and C_{deep} are non-overlapped with each other and diagnosed following the relationships,

$$C_{conv} q^*\left(T_c\right) + \left(1 - C_{conv}\right)\overline{q} = \overline{q}_{conv} \tag{4}$$

$$C_{conv} T_c + \left(1 - C_{conv}\right)\overline{T} = \overline{T}_{conv} \tag{5}$$

and

$$q^*\left(T_c\right) = q^*\left(\overline{T}\right) + \frac{\partial q^*\left(\overline{T}\right)}{\partial \overline{T}}\left(T_c - \overline{T}\right) \tag{6}$$

where $\bar{q}$ and $\bar{T}$, $\bar{q}_{conv}$ and $\bar{T}_{conv}$ denote the model grid box-averaged water vapor mixing ratio and temperature in the 'environment' before and after convection activity, respectively. T_c and $\mathrm{q}^*(T_c)$ are the temperature inside the convective cloud plume and its saturated water vapor mixing ratio. Here, we assume that the shallow and deep convection can concurrently occur in the same atmospheric column at any time step. That is, the shallow convection scheme follows the deep convection and occurs at vertical layers where local instability still remains after deep convection.

If no supersaturation exists in clouds, we can obtain from Eqs. (4) and (5)

$$C_{conv} = \frac{\left(\bar{q}_{conv} - \bar{q}\right) - \dfrac{\partial q^*\left(\bar{T}\right)}{\partial \bar{T}}\left(\bar{T}_{conv} - \bar{T}\right)}{q^*\left(\bar{T}\right) - \bar{q}}. \tag{7}$$

The temperature T_c and the specific humidity $q_c = \mathrm{q}^*(T_c)$ of the cloud plume can be firstly derived from Eqs. (5) and (6). Following the method above, the cloud fraction (C_{deep} and $C_{shallow}$), temperature (T_{deep} and $T_{shallow}$), specific humidity (q_{deep} and $q_{shallow}$) for the deep convective, shallow convective clouds can be then deduced sequentially.

After the three moisture processes (i.e. deep convection, then shallow convection, and finally stratiform precipitation) are finished, the mean temperature ($\overline{\mathrm{T}}_{\mathrm{box}}$) and specific humidity ($\bar{\mathrm{q}}_{\mathrm{box}}$) of the whole model-grid box are then updated. Ambient temperature ($\overline{\mathrm{T}}_{\mathrm{ambient}}$) and specific humidity ($\bar{\mathrm{q}}_{\mathrm{ambient}}$) outside convective clouds can be finally estimated using the following Eqs.,

$$\bar{q}_{box} = \bar{q}_{ambient} \cdot \left(1 - C_{deep} - C_{shallow}\right) + q_{deep} \cdot C_{deep} + q_{shallow} \cdot C_{shallow}, \tag{8}$$

and

$$\bar{T}_{box} = \bar{T}_{ambient} \cdot \left(1 - C_{deep} - C_{shallow}\right) + T_{deep} \cdot C_{deep} + T_{shallow} \cdot C_{shallow}. \tag{9}$$

Finally, the stratus cloud fraction $\mathrm{C_S}$ is diagnosed on the basis of the relative humidity ($RH_{ambient}$) of the ambient,

$$C_s = \left(\frac{RH_{ambient} - RH_{\min}}{1 - RH_{\min}}\right)^2 \tag{10}$$

where RH_{min} is a threshold of relative humidity and $RH_{ambient}$ is derived with $\overline{T}_{ambient}$ and $\overline{q}_{ambient}$. If $C_{deep} + C_{shallow} > 1$ in Eqs. (8) and (9), C_{deep} and $C_{shallow}$ are scaled to meet the condition $C_{deep} + C_{shallow} = 1.0$, and then $C_s = 0$. At that condition, we do not calculate $\overline{T}_{ambient}$ and $\overline{q}_{ambient}$ from Eqs. (8) and (9).

d. Cloud microphysics

In BCC-AGCM2.2 and BCC-AGCM3-MR, the essential part of the stratiform cloud microphysics remains the same and follows the framework of non-convective cloud processes in CAM 3.0 (Collins et al., 2004) that is the scheme proposed by Rasch and Kristj ánsson (1998) and modified by Zhang et al. (2003). However there is a noticeable difference of cloud microphysics in the two models concerning the treatments for indirect effects of aerosols through mechanisms of clouds and precipitation. Indirect effects of aerosols were not included in BCC-AGCM2.2 for CMIP5. That is, the cloud droplets effective radius was not related to aerosols, neither the precipitation efficiency. The cloud droplets effective radius was either prescribed or a simple function of atmospheric temperature. The effective radius for warm clouds was specified to be 14 μ m over open ocean and sea ice, and was a function of atmospheric temperature over land. For ice clouds, the effective radius was also a function of temperature following Kristj ánsson et al. (2000).

Aerosol particles influence clouds and the hydrological cycle by their ability to act as cloud condensation nuclei and ice nuclei. This indirect radiative forcing of aerosols is included in the latest version of BCC-AGCM3-MR, with the effective radius of liquid water cloud droplets being related to the cloud droplet number concentration N_{cdnc} (cm^{-3}). As proposed by Martin et al. (1994), the volume-weighted mean cloud droplet radius $r_{l,vol}$ can be expressed as

$$r_{l,vol} = \left[(3LWC) / (4\pi \rho_w N_{cdnc}) \right]^{1/3}, \tag{11}$$

where ρ_w is the liquid water density, LWC is the cloud liquid water content (g cm^{-3}). Cloud water and ice contents are prognostic variables in our model with source and sink terms taking into account the cloud microphysics. The effective radius of cloud droplets r_{el} is then estimated as

$$r_{el} = \beta \cdot r_{l,vol} \tag{12}$$

where β is a parameter dependent on the droplets spectral shape. There are various methods to parameterize it (e.g. Pontikis and Hicks, 1992; Liu and Daum, 2002). We use the calculation proposed by Peng and Lohmann (2003),

$$\beta = 0.00084 N_{cdnc} + 1.22 \tag{13}$$

In BCC-AGCM3-MR, the liquid cloud droplet number concentration N_{cdnc} (cm^{-3}) is a diagnostic variable dependent on aerosols mass. It is explicitly calculated with the empirical function suggested by Boucher and Lohmann (1995) and Quaas et al. (2006) :

$$N_{cdnc} = \exp\left[5.1 + 0.41\ln\left(m_{aero}\right)\right] \tag{14}$$

The total aerosols mass is the sum of four types of aerosol,

$$m_{aero} = m_{SS} + m_{OC} + m_{SO_4} + m_{NH_4NO_2} . \tag{15}$$

Here, m_{aero} ($\mu g.m^{-3}$) is the total mass of all hydrophilic aerosols, i.e., the first bin (0.2 to 0.5 μm) of sea salt (m_{SS}), hydrophilic organic carbon (m_{OC}), sulphate (m_{SO_4}), and nitrate ($m_{NH_4NO_4}$). Nitrate as a rapidly increasing aerosol species in recent years affects present climate and potentially has large implications on climate change (Xu and Penner, 2012; Li et al., 2014). A dataset of nitrate from NCAR CAM-Chem (Lamarque et al., 2012) is used in our model.

Aerosols also exert impacts on precipitation efficiency (Albrecht, 1989), which is taken into account in the parameterization of non-convective cloud processes. We use the same scheme as in CAM3 (Rasch and Kristj ánsson, 1998; Zhang et al., 2003). There are five processes that convert condensate to precipitate: auto-conversion of liquid water to rain, collection of cloud water by rain, auto-conversion of ice to snow, collection of ice by snow, and collection of liquid by snow. The auto-conversion of cloud liquid water to rain (PWAUT) is dependent on the cloud droplet number concentration and follows a formula that was originally suggested by Chen and Cotton [1987],

$$PWAUT = C_{l,aut} q_l^2 \rho_a / \rho_w \left(\frac{q_l \rho_a}{\rho_w N_{ncdc}} \right)^{1/3} H\left(r_{l,vol} - r_{lc,vol}\right) \tag{16}$$

Where $\hat{q}_l$ is in-cloud liquid water mixing ratio, ρ_a and ρ_w are the local densities of air and water respectively, and

$$C_{l,aut} = 0.55\pi^{1/3} k (3/4)^{4/3} (1.1)^4 . \quad (17)$$

In which k = 1.18 $\times$ 10^6 cm^{-1} sec^{-1} is the Stokes constant. H(x) is the Heaviside step function with the definition,

$$H(x) = \begin{cases} 0, & x < 0 \\ 1, & x \geq 0 \end{cases} \quad (18)$$

$r_{lc,vol}$ is the critical value of mean volume radius of the liquid cloud droplets $r_{l,vol}$, and set to 15 μ m.

e. Gravity wave drag

Gravity waves can be generated by a variety of sources including orography, convection, and geostrophic adjustment in regions of baroclinic instability (Richter et al., 2010). Gravity waves propagate upward from their source regions and break when large amplitudes are attained. This produces a drag on the mean flow. Gravity wave drag plays an important role in explaining the zonal mean flow and thermal structure in the upper atmosphere.

In previous versions of BCC models, the orographic gravity wave drag was parameterized as in McFarlane (1987), but non-orographic sources were not considered. In BCC-AGCM3-MR, the gravity wave drag generated from convective sources is introduced as in Beres et al. (2004), but drag by blocking effects is still not involved. The key point of the Beres' scheme is relating the momentum flux phase speed spectrum to the convective heating properties. In the present version of BCC-AGCM3-MR, the convective gravity wave parameterization is activated only when the deep convective heating depth is greater than 2.5 km.

The uncertainty in the magnitude of momentum flux arises from the horizontal scale of the heating and the convective fraction. The convective fraction (CF) within a grid cell is an important parameter and can be tuned to obtain right wave amplitudes. It is a constant and valid for all latitudes where convection is active. Previous studies of Alexander et al. (2004) show that CF can vary from ~0.2% to ~7%–8%. We use 5% in BCC-AGCM3-MR. This parameterization scheme of convective gravity waves can improve the model's ability to simulate the stratospheric quasi-biennial oscillation in BCC-AGCM3-MR.

f. Radiative transfer

The radiative transfer parameterization in BCC-AGCM2.2 follows the scheme initially implemented in CAM3 (Collins et al., 2004). Aerosol indirect effects on radiation are not taken into account and cloud droplets effective radius is only function of temperature for cold clouds and prescribed to different values for maritime, polar, and continental cases for warm clouds. In BCC-AGCM3-MR, however, the aerosol indirect effects are fully included and the effective radius of droplets for liquid clouds is calculated by Equation (12) using the liquid cloud droplet number concentration.

g. Boundary layer turbulence

BCC-AGCM3-MR basically inherits the boundary layer turbulence parameterization used in BCC-AGCM2.2, which is based on the eddy diffusivity approach (Holtslag and Boville, 1993). The eddy diffusivity is given by

$$K_c = k w_t z \left(1 - \frac{z}{h}\right)^2, \tag{19}$$

where w_t is a turbulent velocity and *h* is the boundary layer height, which is estimated as

$$h = z_s + \frac{Ri_c \left\{ \left[u(h) - u_{SL}\right]^2 + \left[v(h) - v_{SL}\right]^2 + \beta u_*^2 \right\}}{(g/\theta_{SL})\left[\theta_v(h) - \theta_{SL}\right]}, \tag{20}$$

where z_s is the height of the lowest model level, *u*, *v*, and θ_v are horizontal wind components and virtual potential temperature at height *z*, u_{SL}, v_{SL}, and θ_{SL} represent the same variables, but in the surface layer. β in Eq. (20) is a constant and taken as 100. u_* is the friction velocity, and *g* is gravitational acceleration.

The critical Richardson number Ri_c in Eq. (20) is a key parameter for calculating the boundary layer height and is set to a constant (0.3) for all stable conditions in BCC-AGCM2.2. In BCC-AGCM3-MR, Ri_c varies according to conditions of boundary layer stability to yield more accurate estimates of boundary layer height, and set to 0.24 for strongly stable conditions, 0.31 for weakly stable conditions, and 0.39 for unstable conditions based on observational studies of Zhang et al. (2014).

2.2 Land component BCC-AVIM

BCC-AVIM, Beijing Climate Center Atmosphere-Vegetation Interaction Model, is a

288 comprehensive land surface scheme developed and maintained in BCC. The version 1 (BCC-AVIM1.0)
289 was used as the land component in BCC-CSM1.1m participating in CMIP5 (Wu et al., 2013). It
290 includes major land surface biophysical and plant physiological processes. Its origin could go back to
291 the Atmosphere-Vegetation Interaction Model (AVIM) (Ji, 1995; Ji et al., 2008) with the necessary
292 framework to include biophysical, physiological, and soil carbon-nitrogen dynamical processes. The
293 biophysical module in BCC-AVIM1.0, with 10 layers for soil and up to five layers for snow, is almost
294 the same as that used in the NCAR Community Land Model version 3 (CLM3) (Oleson et al., 2004).
295 The terrestrial carbon cycle in BCC-AVIM1.0 consists of a series of biochemical and physiological
296 processes modulating photosynthesis and respiration of vegetation. Carbon assimilated by vegetation is
297 parameterized by a seasonally varying allocation of carbohydrate to leaves, stem, and root tissues as a
298 function of the prognostic leaf area index. Litter due to turnover and mortality of vegetation, and carbon
299 dioxide release into atmosphere through the heterogeneous respiration of soil microbes is taken into
300 account in BCC-AVIM1.0. Vegetation litter falls to the ground surface and into the soil is divided into
301 eight idealized terrestrial carbon pools according to the timescale of carbon decomposition of each pool
302 and transfers among different pools, which is similar to that in the carbon exchange between vegetation,
303 soil and the atmosphere (CEVSA) model (Cao and Woodward, 1998).

304 BCC-AVIM1.0 has been updated to BCC-AVIM2.0 which serves as the land component of
305 BCC-CSM2-MR participating in CMIP6. As listed in Table 3, several improvements have been
306 implemented in BCC-AVIM2.0, such as the inclusion of a variable temperature threshold to determine
307 soil water freezing/thawing rather than fixed at 0°C, a better calculation of snow surface albedo and
308 snow cover fraction, a dynamic phenology for deciduous plant function types, and a four-stream
309 approximation on solar radiation transfer through vegetation canopy. Besides, a simple scheme for
310 surface fluxes over rice paddy is also implemented in BCC-AVIM2.0. These improvements are briefly
311 discussed as follows.

312 (a) Soil water freezes at the constant temperature 0℃ in BCC-AVIM1.0, but the actual
313 freezing-thawing process is a slowly and continuously changing process. We take into account the fact
314 that the soil water potential remains in equilibrium with the water vapor pressure over pure ice when
315 soil ice is present. Based on the relationships among soil water matrix potential ψ (mm), soil

temperature and soil water content, a variable temperature threshold for freeze-thaw dependent on soil liquid water content, soil porosity and saturated soil matrix potential is introduced. The inclusion of this scheme improves the performance of BCC-AVIM2.0 in the simulation about seasonal frozen soil (Xia et al., 2011).

(b) In BCC-AVIM1.0, we took into account the snow aging effect on surface albedo with a simple consideration by using a unified scheme to mimic the snow surface albedo decrease with time. In BCC-AVIM2.0, we assume different reduction rates of snow albedo with actual elapsed time after snowfalls in the accumulating and melting stages of a snow season (Chen et al., 2014). Besides, the variability of sub-grid topography is now taken into account to calculate the snow cover fraction within a model grid cell.

(c) Unlike the empirical plant leaf unfolding and withering dates prescribed in BCC-AVIM1.0, a dynamic determination of leaf unfolding, growth, and withering dates according to the budget of photosynthetic assimilation of carbon similar to the phenology scheme in CTEM (Arora, 2005) was implemented in BCC-AVIM2.0. Leaf loss due to drought and cold stresses in addition to natural turnover are also considered.

(d) The four-stream solar radiation transfer scheme within canopy in BCC-AVIM2.0 is based on the same radiative transfer theory used in atmosphere (Liou, 2004). It adopts the analytic formula of Henyey-Greenstein for the phase function. The vertical distribution of diffuse light within canopy is related to transmisivity and reflectivity of leaves, besides, average leaf angle and direction of incident direct beam radiation influence diffuse light within canopy as well. The upward and downward radiative fluxes are determined by the phase function of diffuse light, G-function, leaf reflectivity and transmisivity, leaf area index, and the cosine of solar angle of incident direct beam radiation (Zhou et al., 2018).

(e) Considering the wide distribution of rice paddies in Southeast Asia and the quite different characteristics of rice paddies and bare soil, a scheme to parameterize the surface albedo, roughness length, turbulent sensible and latent heat fluxes over rice paddies is developed (a manuscript is in preparation) and implemented in BCC-AVIM2.0.

(f) Finally, land-use and land-cover changes are explicitly involved in BCC-AVIM2.0. An increase

in crop area implies the replacement of natural vegetation by crops, which is often known as deforestation.

2.3 Ocean and Sea Ice

There are no significant changes for the ocean and sea ice from BCC-CSM1.1m to BCC-CSM2-MR. But for the sake of completeness, we present here a short description of them. The oceanic component is MOM4-L40, an oceanic GCM. It was based on the Z-coordinate Modular Ocean Model (MOM), version 4 (Griffies, 2005) developed by the Geophysical Fluid Dynamics Laboratory (GFDL). It has a nominal resolution of 1 °×1 ° with a tri-pole grid, the actual resolution being from 1/3 ° latitude between 30 °S and 30 °N to 1.0 ° at 60 ° latitude. There are 40 z-levels in the vertical. The two northern poles of the curvilinear grid are distributed to land areas over Northern America and over the Eurasian continent. There are 13 vertical levels placed between the surface and the 300-m depth of the upper ocean. MOM4_L40 adopts some mature parameterization schemes, including Swedy's tracer-based third order advection scheme, isopycnal tracer mixing and diffusion scheme (Gent and McWilliams, 1990), Laplace horizontal friction scheme, KPP vertical mixing scheme (Large et al., 1994), complete convection scheme (Rahmstorf, 1993), overflow scheme of topographic processing of sea bottom boundary/steep slopes (Campin & Goosse, 1999), and shortwave penetration schemes based on spatial distribution of chlorophyll concentration (Sweeney et al., 2005).

Concentration and thickness of sea ice are calculated by the Sea Ice Simulator (SIS) developed by GFDL (Winton, 2000). It is a global sea ice thermodynamic model including the Elastic–Viscous–Plastic dynamic process and Semtner's thermodynamic process. SIS has 3 vertical layers, including 1 snow cover and 2 ice layers of equal thickness. In each grid, 5 categories of sea ice (including open water) are considered, according to the thickness of sea ice. It also takes into account the mutual transformation from one category to another under thermodynamic conditions. The sea ice model operates on the same oceanic grid and has the same horizontal resolution of MOM_L40. SIS calculates concentration, thickness, temperature, salinity of sea ice and motions of snow cover and ice sheet. There is no gas exchange through sea ice.

2.4. Surface turbulent fluxes between air and sea/sea ice

The atmosphere and sea/sea ice interplay through the exchange of surface turbulent fluxes of

momentum, heat and water. An optimum treatment of the surface exchange, sound in physics and economic in computation, is very important in simulating the climate variability. During the past years, we maintain a continuous effort to improve the turbulent exchange processes between air and sea/sea ice in different versions of BCC models.

In BCC-CSM1.1m, the bulk formulas of turbulent fluxes over sea surface originate from those used in CAM3, with some modifications to the roughness lengths and corrections to the temperature and moisture gradients considering sea spray effects (Wu et al., 2010). The bulk formulas are updated in BCC-CSM2-MR. The coefficients in roughness lengths calculations were adjusted and the arbitrary gradient corrections are not used. Instead, a gustiness parameterization is included to account for the subgrid wind variability that is contributed by boundary layer eddies, convective precipitation, and cloudiness (Zeng et al., 2002).

In terms of turbulent exchange between air and sea ice, we proposed a new bulk algorithm aiming to improve flux parameterizations over sea ice (Lu et al., 2013). Based on theoretical and observational analysis, the new algorithm employs superior stability functions for stable stratification as suggested by Zeng et al. (1998), and features varying roughness lengths. All the three roughness lengths (z_0, z_T, z_Q) of sea ice were set to a constant (0.5 mm) in BCC-CSM1.1m. Observational studies show that values of z_0 tend to be smaller than 0.5 mm over sea ice in winter and larger than 0.5 mm in summer (Andreas et al., 2010a; Andreas et al., 2010b). In the new parameterization used in BCC-CSM2-MR, the roughness lengths for momentum differentiate between warm and cold seasons. For simplicity, z_0 is treated as

$$z_0\left(mm\right)=\begin{cases}0.1 & \text{for } T_s \le -2°C \\ 0.8 & \text{for } T_s > -2°C\end{cases}, \tag{19}$$

where T_s represents surface temperature. For the scalar roughness lengths, a theoretical-based model proposed by Andreas (1987) is used in the new scheme. This model expresses the scalar roughness z_s (z_T or z_Q) as a function of the roughness Reynolds number R*, i.e.,

$$\ln\left(z_s/z_0\right)=b_0+b_1\left(\ln R_*\right)+b_2\left(\ln R_*\right)^2. \tag{20}$$

Andreas (1987, 2002) tabulates the polynomial coefficients b_0, b_1 and b_2.

3. Experimental design

All BCC simulations presented in this work follow the protocols defined by CMIP5 and CMIP6.

We pay attention for them to be comparable in spite of showing the transition of our climate system model from CMIP5 to CMIP6. The principal simulation to be analyzed is the historical simulation (hereafter historical) with prescribed forcings from 1850 to 2005 for CMIP5 (to 2014 for CMIP6).

Historical forcings data are based as far as possible on observations and downloaded from the webpage (https://esgf-node.llnl.gov/search/input4mips/). They mainly include: (1) GHG concentrations (only CO_2, N_2O, Ch_4, CFC11, CFC12 used in BCC models) with zonal-mean values and updated monthly; (2) Yearly global gridded land-use forcing; (3) Solar forcing; (4) Stratospheric aerosols (from volcanoes); (5) CMIP6-recommended anthropogenic aerosol optical properties which is formulated in terms of nine spatial plumes associated with different major anthropogenic source regions (Stevens et al., 2017). (6) Time-varying gridded ozone concentrations. In addition, aerosol masses based on CMIP5 (Taylor et al., 2012) are used for on-line calculation of cloud droplet effective radius in BCC model.

The preindustrial initial state of BCC-CSM2-MR is preceded by a 500-years piControl simulation following the requirement of CMIP6. The initial state of the piControl simulation itself is obtained through individual spin-up runs of each component of BCC-CSM2-MR in order for piControl simulation to run stably and fast to its model equilibrium. Actually, the initial states of atmosphere and land are obtained from a 10-years AMIP run forced with monthly climatology of sea surface temperature (SST) and sea ice concentration, and the initial states of ocean and sea ice are derived from a 1000-years forced run with a repeating annual cycle of monthly climatology of atmospheric state from the Coordinated Ocean-Ice Reference Experiment (CORE) dataset version 2 (Danabasoglu et al., 2014). Figure 2 shows time series of the annual and global mean of net energy flux at top of the atmosphere and the sea surface temperature for 600 years in the piControl simulation. The whole system in BCC-CSM2-MR nearly reaches its equilibrium after 600 years.

4. Evaluation and comparison between BCC CMIP5 and CMIP6 models

4.1 Global Energy Budget

Radiative fluxes at the top of the model atmosphere are fundamental variables characterizing the Earth's energy balance. Satellite observations in modern time allow us to monitor changes in the net radiation at top-of-atmosphere (TOA) from 2001 onwards. CERES (Clouds and Earth's Radiant Energy System) project, with the lessons learned from its predecessor, the Earth's Radiation Budget Experiment

(ERBE), provides improved observation-based data products of Earth's radiation budget (Wielicki et al, 1996). Recently, data of CERES are synthesized with EBAF (Energy Balanced and Filled) data to derive the CERES-EBAF products, suitable for evaluation of climate models (Loeb et al., 2012). As shown in Table 4, the TOA shortwave and longwave components in BCC-CSM2-MR are generally closer to CERES-EBAF compared to those in BCC-CSM1.1m. Model results are for the period 1986–2005, while the available CERES-EBAF data are for 2003–2014. Globally-averaged TOA net energy is 0.85 W m^{-2} in BCC-CSM2-MR and 0.98 W m^{-2} in BCC-CSM1.1m for the period from 1986 to 2005. The energy equilibrium of whole earth system in BCC-CSM2-MR is slightly improved.

Clouds constitute a major modulator of the radiative transfer in the atmosphere for both solar and terrestrial radiations. Their macro and micro properties, including their radiative properties exert strong impacts on the equilibrium and variation of the radiative budget at TOA or at surface. Figure 3 displays annual and zonal mean of shortwave, longwave and net cloud radiative forcing for BCC CMIP5 (blue curves), CMIP6 (red curves) models and observations (black curves). The data used in Fig. 3 are the same as in Table 4. Although observations and models results cover different time periods, they are still relevant to reveal climatological mean performance of climate models. In low latitudes between 30 ℃S and 30 ℃N, BCC-CSM1.1m shows excessive cloud radiative forcing for both shortwave and longwave radiations. These biases are largely reduced in BCC-CSM2-MR, which is possibly attributed to the new algorithm of cloud fraction especially for convective cloud amount. Cloud radiative forcing in mid latitudes shows large uncertainty, also manifested in the large deviation between the two observations. Cloud radiative forcing in both models is closer to CERES-EBAF than to CERES in mid latitudes. It is clear that the new physics modifies the simulated climate and cloud properties, including the fractional coverage of clouds, their vertical distribution as well as their liquid water and ice content.

4.2. Performance in Simulating the Global Warming in the 20th Century

The historical simulation allows us to evaluate the ability of models to reproduce the global warming and climate variability in the 20th century. The performance depends on both model formulation and the time-varying external forcings imposed on the models (Allen et al., 2000). Figure 4 presents global-mean (from 60 ℃S to 60 ℃N) surface air temperature evolutions from HadCRUT4 (Morice et al., 2012) and BCC CMIP5 and CMIP6 models. Here only the area from 60° S to 60 ℃N is used for

comparison, since few observations existed in polar regions to deduce reliable information in HadCRUT4, especially before the 20th century. To better reveal long-term trends, the climatological mean is calculated for the reference period 1961–1990 and removed from the time series. The interannual variability of both simulations is qualitatively comparable to that observed. When a 9-year smoothing is applied, the long-term trend of both CMIP6 and CMIP5 models is highly correlated with HadCRUT4. Figure 4 presents three members of historical simulations from different initial state of the piControl simulation. The correlation coefficients are 0.90 in CMIP5 and 0.93, 0.93, 0.90 in three members of CMIP6, respectively.

A remarkable feature in Figure 4 is the presence of a global warming hiatus or pause for the period from 1998 to 2013 when the observed global surface air temperature warming slowed down. This is a hot topic, largely debated in the scientific research community (e.g. Fyfe et al., 2016; Medhaug et al., 2017). There are two members (r1i1p1f1 and r2i1p1f1 in Fig. 4) of historical simulations of the CMIP6 model show a hiatus towards the end of the simulation that resembles the observed one, and the third member (r3i1p1f1) shows a decreased trend of warming in the same period. Another warming hiatus occurred in the period of 1942 to 1974. The first and the third members (r1i1p1f1 and r3i1p1f1) of BCC-CSM2-MR only simulate the warming slowdown in the late period from 1958 to 1974, but the second member (r2i1p1f1) of BCC-CSM2-MR almost simulate this warming hiatus in the whole period from 1942 to 1974. The reason why the BCC CMIP6 model simulates both periods of global warming hiatus is beyond the scope of this paper and will be explored in future.

The models response of the SAT to volcanic forcing is slightly stronger than that estimated with HadCRU data. Evident global cooling shocks are coincident with significant volcanic eruptions such as Krakatoa (in 1883), West Indies Agung (in 1963), and Mount Pinatubo (in 1991). Each of these volcanic eruptions significantly enriched stratospheric aerosols (available from http://data.giss.nasa.gov/modelforce/strataer/). As shown in Figure 4, SAT may decrease by up to 0.4 ℃ within 1 to 2 years after major volcanic eruptions. The substantial cooling response to volcanic eruptions is, to a great extent, due to the aerosol direct radiative forcing too strong in both versions of BCC-CSM.

To keep the paper concise and at a reasonable length, only the first member of CMIP6 historical

simulations of BCC-CSM2-MR will be presented hereafter. Biases of annual mean surface air temperature (at 2 meters) in the whole globe for BCC-CSM2-MR and BCC-CSM1.1m are shown in Figure 5. In both BCC models, biases are generally within ±3℃, but there are slightly systematic warm biases over oceans from 50℃S to 50℃N and systematic cold ones over most land regions in north of 50℃N, in East Asia and in North Africa. Cold biases in high latitudes of the Northern Hemisphere (North Atlantic, Arctic, North America and Siberia) seem amplified in BCC-CSM2-MR. The land surface biases in both coupled models are similar to each other. Those patterns of biases are already present in AMIP simulations (not shown), where effects of oceanic biases are excluded. So those biases in land surface partly come from their land surface modelling component. In the Southern Ocean, both models show a strong warm area in the Weddell Sea. BCC-CSM1.1m shows cold biases in other regions of the Southern Ocean. The disappearance of cold biases in the Southern Oceans in BCC-CSM2-MR is possibly attributed to the new scheme of cloud fraction (Table 2) as there is a zone of low-level cloud between 40℃S to 60℃S in the Southern Ocean (omitted), not only in models but also in observations.

4.3 Climate sensitivity to CO_2 increasing

The long trend of global warming in Figure 4 depends on the climate sensitivity which is an emblematic parameter to characterize the sensitivity of a climate model to external forcing, with all feedbacks included. It generally designates the variation of global mean surface air temperature in response to a forcing of doubled CO_2 concentration in the atmosphere (IPCC 2013). As commonly practiced in the climate modelling community, an equilibrium climate sensitivity and a transient climate response can be separately evaluated, corresponding to a situation of equilibrium and transient states of climate.

We use the standard simulation of 1% CO_2 increase per year (1pctCO_2) to calculate the transient climate response (TCR), while the equilibrium climate sensitivity (ECS) uses the 4xCO_2 abrupt-change simulation by applying the forcing/response regression methodology proposed by Gregory et al. (2004). The TCR is calculated using the difference of annual surface air temperature between the pre-industrial experiment and a 20-year period centered on the time of CO_2 doubling in 1pctCO_2, which is 1.71 for BCC-CSM2-MR and 2.02 for BCC-CSM1.1m. The ECS is diagnosed from the 150-year run of abrupt

511 4xCO2 following the approach of Gregory (2012). The method is based on the linear relationship
512 (Figure 6) governing the changes of net top-of-atmosphere downward radiative flux and the surface air
513 temperature simulated in abrupt $4xCO_2$ relative to the pre-industrial experiment. The ECS is equal to a
514 half of the temperature change when the net downward radiative flux reaches zero (Andrews et al.,
515 2012). It is assumed here that $2xCO_2$ forcing is half of that for $4xCO_2$, hypothesis generally verified in
516 climate models. As shown in Fig. 6, the ECS is 3.03 for BCC-CSM2-MR and 2.89 for BCC-CSM1.1m.
517 So the TCR of the new version model BCC-CSM2-MR is lower than BCC-CSM1.1m, but the ECS of
518 BCC-CSM2-MR is slightly higher than BCC-CSM1.1m.

519 The linear regression line shown in Figure 6, as pointed out in Gregory et al. (2012), also allows
520 estimating the instantaneous forcing due to CO_2 increase, and eventually feedbacks parameter of the
521 climate system. The former is the cross point of the linear regression line with Y axis: 6.2 $W \cdot m^{-2}$ for
522 BCC-CSM2-MR and 7.6 $W \cdot m^{-2}$ for BCC-CSM1.1m. They can be scaled to the case of $2xCO_2$ just with
523 a division factor of 2. Since ECS values are close to each other in the two models, we can easily deduce
524 that all-feedback factor is larger in BCC-CSM2-MR than in BCC-CSM1.1m. It is actually not
525 surprising to see differences of $2xCO_2$ radiative forcing between the two models even the radiative
526 transfer scheme is kept identical, because changes in 3-D structures of cloud, atmospheric temperature
527 and water vapor do exert impacts on additional radiative forcing due to CO_2 increase in the atmosphere.
528 It is however interesting to note that feedbacks can operate, in the two models, in such a different way
529 that ECS keeps almost unchanged between them.

530 **4.4 Behaviors of the atmosphere at present day**

531 The main spatial patterns of observed precipitation climatology are simulated in BCC-CSM1.1m
532 and BCC-CSM2-MR. Figure 7 shows model biases of annual-mean precipitation for BCC-CSM1.1m
533 and BCC-CSM2-MR in the globe. They are very close from each other. Their RMSE is also very close:
534 1.12 mm/day against 1.18 mm/day. Regions of lack of precipitation, such as North India, South China,
535 the two sides of Sumatra, and the Amazon, experience significant amelioration in the new model.
536 Excessive rainfalls in Tropical Africa, in the Indian Ocean, in the Maritime Continent seem amplified in
537 BCC-CSM2-MR. As for the whole globe, the annual mean precipitation coming from convective
538 process (including deep and shallow convections) accounts for 50% of the total precipitation (2.94

539 mm/day) in BCC-CSM2-MR and 48% of the total precipitation (2.87 mm/day) in BCC-CSM1.1m. The
540 convective precipitation increased in BCC-CSM2-MR, and the total amount of precipitation exceeds the
541 amount (2.68 mm/day) of 1986-2005 mean observed precipitation analyses from Global Precipitation
542 Climatology Project (Adler et al., 2003). But in some regions such as in the Maritime Continent, stratus
543 precipitation evidently enhances in BCC-CSM2-MR, where the ratio of convection precipitation to total
544 precipitation is 39% and even larger than 35% in BCC-CSM1.1m.

545 We now use the Taylor diagram (Figure 8) to evaluate the general performance of our two models
546 in terms of temperature at 850hPa, precipitation and atmospheric general circulation. The evaluation is
547 done against climatology of ERA-Interim dataset for the period of 1986 to 2005 (Dee et al., 2011).
548 ERA-Interim is the latest global atmospheric reanalysis produced by the European Centre for
549 Medium‐Range Weather Forecasts (ECMWF).

550 For global fields, we calculate the spatial pattern correlations between models and ERA-Interim
551 dataset for the annual-mean climatology of sea level pressure (SLP), temperature at 850 hPa level
552 (T850), wind velocity at 850 hPa (U850 and V850) and at 200 hPa (U200), and geopotential height at
553 500hPa (Z500), and Global Precipitation Climatology Project dataset of precipitation (PRCP in Fig. 8,
554 Adler and Chang, 2003) over the period 1980–2000. Except for precipitation and zonal wind at 850 hPa
555 which have lower correlation (less than 0.90) with observation, correlations for other variables are all
556 above 0.90. The pattern correlation of geopotential height at 500hPa with ERA-Interim is 0.995, the
557 best correlation among these variables. Except for V850, correlations of all other variables in CMIP6
558 model version (BCC-CSM2-MR) have an evident improvement compared to CMIP5 version
559 (BCC-CSM1.1m). The normalized standard deviations of most variables except for the precipitation
560 and T850 are obviously improved in BCC-CSM2-MR. As a whole, the performances of most variables
561 in BCC-CSM2-MR are better than those in BCC-CSM1.1m.

562 Results shown in the Taylor diagrams in Figure 8 about improvements in surface climate and
563 atmospheric general circulation at different vertical levels are consistent with improvements in the
564 vertical distribution of atmospheric temperature. Figure 9 shows the yearly-averaged zonal mean of
565 atmospheric temperature biases in BCC-CSM2-MR and BCC-CSM1.1m, with ERA-Interim for the
566 period of 1986–2005 as reference. Overall, both BCC-CSM2-MR and BCC-CSM1.1m have similar

biases in their vertical structure, with 1–3 K warmer in the stratosphere (above 100 hPa) for most of the domain equatorward of 70 ℃N and 70 ℃S. There are larger cold biases near the tropopause (centered near 200hPa) for southward of 30 ℃S and northward of 30 ℃N. In the middle to lower troposphere (below 400hPa), there is a warm bias of 1-2K. Improvements in BCC-CSM2-MR are mainly located in the troposphere below 100 hPa. Both cold biases near the tropopause in high latitudes and warm bias in lower latitudes are reduced.

The improvement in tropospheric temperature induces naturally smaller biases for the zonal wind in the whole troposphere in BCC-CSM2-MR (Figure 9). But there are still westerly wind biases of 6 $m \cdot s^{-1}$ in the layer of 100-200 hPa in the tropics. Westerly jets at mid-latitudes are slightly too strong in both hemispheres. The zonal mean of zonal wind biases in the high latitudes of the stratosphere in BCC-CSM2-MR have increased near 10 hPa, where model biases may be partly caused by not yet involved gravity wave drag that generated by blocking effects. We expect to reduce this model bias in next version by adding this process.

Given a much higher vertical resolution and an advanced parameterization of the gravity wave drag, the new model BCC-CSM2-MR is able to represent the stratospheric quasi-biennial oscillation (QBO), as shown in Figure 10 which displays time-height diagrams of the tropical zonal winds averaged from 5 ℃S to 5 ℃N. The three panels show observations from the ERA-Interim reanalysis and relevant simulation results from the two models in CMIP6 and CMIP5. Figure 10a shows alternative westerlies and easterlies in the lower stratosphere appearing with a mean period of about 28 months in the ERA-Interim reanalysis. In Figure 10b, the BCC-CSM2-MR simulations present a clear quasi-biennial oscillation of the zonal winds as observed. In this study, the QBO period is taken as the time between easterly and westerly wind transitions at 20 hPa. The simulation produces about 12 QBO cycles from 1980 to 2005. The average period is 24.6 months, whereas the shortest and longest cycles last for 18 and 35 months, respectively. ERA-Interim values are 27.9, 23, and 35 months for average, minimum, and maximum of cycle length. The observed asymmetry in amplitude with the easterlies being stronger than the westerlies is reproduced in the simulated zonal winds. At 20 hPa, the simulated easterlies often exceed -20 $m\ s^{-1}$, while in the reanalysis easterly winds peak at -30 to -40 $m\ s^{-1}$. Simulated westerlies of the QBO range from 8 to 12 $m\ s^{-1}$, whereas the reanalysis show peak winds of

16 to 20 m s^{-1}. The amplitudes of the QBO cycles in the simulation are weaker than in the reanalysis, which is possibly due to inadequate gravity wave forcing to drive the QBO. The downward propagation of the simulated QBO phases occurs in a regular manner, but does not penetrate to sufficiently low altitudes. It may depend on the vertical resolution and the impact of vertical resolution on downward propagation will be discussed in a separate paper. After a few test of model vertical layers, we tend to conclude that 46 vertical layers (Figure 1) seem the minimum number to simulate QBO in BCC-CSM2-MR. In BCC-CSM1.1m, however, as shown in Figure 10c, QBO is inexistent and only a semiannual oscillation of easterlies can be found.

Madden-Julian Oscillation (MJO) is a very important atmospheric variability acting within a periodicity between 20 and 100 days in the tropics with considerable effects on regional weather and climate. It exerts significant impacts on monsoonal circulations and organization of tropical rainfalls. From the tropical Indian Ocean to the Western Pacific, MJO shows a pronounced behavior of eastward propagation, as shown in Figure 11a, in the form of longitude-time, the lagged correlation coefficient of the rainfall in the eastern Indian Ocean (75–85 °E; 5 °S–5 °N) with other positions and with lagged time. We can easily observe the eastward-propagating characteristic, with a moving velocity estimated at 5 m s^{-1}. As shown in a comparison work of Jiang et al. (2015), three fourth of CMIP5 models don't show the propagation behavior, with only a standing oscillation when data are filtered to retain only the 20-100 day variability. Figure 11b and 11c show the same plot, but from our two models in CMIP5 and CMIP6. Although the new model is far from realistic in terms of eastward propagation, there is indeed a clear improvement compared to the old one.

MJO can also exert impacts on weather and climate of extra-tropics, either through emanation of Rossby waves, or the poleward propagation of MJO itself. Figure 11d shows a latitude-time diagram for lagged correlation coefficients when rainfalls are filtered to only retain the variability of 20-100 days. Panels e and f in Figure 11 are the counterpart simulated by our two models. The new model presents a clear improvement.

4.5 Interannual variation of sea surface temperature (SST) in the equatorial Pacific

Figure 12 shows the observed and simulated spatial pattern of standard deviation of SST anomalies in the tropical Pacific. Both BCC-CSM2-MR and BCC-CSM1.1m can simulate the position of the

strongest variation of SST, situated in the central-eastern Pacific in the east of the dateline. However, cold SST in the eastern equatorial Pacific still extends too far west in both models and a cold tongue bias exists in the equatorial Pacific (not shown). As shown in Figure 12a, HadISST observations (Rayner et al., 2003) can clearly identify a zone of large interannual variation of SST from the Peruvian coast to the equatorial cold tongue. It is well simulated in BCC-CSM2-MR, but almost missing in BCC-CSM1.1m.

Figure 13 presents time series of the monthly Nino3.4 SST Index from observations and from simulations of BCC-CSM1.1m and BCC-CSM2-MR. Although amplitudes of interannual variations of the Nino3.4 index in both models are larger than in HadISST observations, it gets weaker in BCC-CSM2-MR with standard deviation of 0.91℃ which is close to observation showing standard deviation of 0.79℃. Recent studies of Lu and Ren (2016) reveal that the period ENSO periodicity in BCC-CSM1.1m is only 2.4 years, much shorter than that in observation. This bias of a too-short periodicity of the ENSO cycle still persists in BCC-CSM2-MR. Lu and Ren (2016) furthermore pointed out that this ENSO periodicity bias in BCC-CSM1.1m is likely caused by an underestimated air-sea coupling strength, and consequently too-weak response of the equatorial Pacific surface westerly wind to SST warm phase in the eastern Pacific. This can affect and distort the zonal advective feedback and thermocline feedback which are two crucial mechanisms for the phase transition of ENSO.

4.6 Sea ice state and oceanic overturning circulation

Figure 14 shows time-series of minimum sea-ice extent from 1851 to 2012 for (a) the Arctic in September and (b) the Antarctic in March as simulated in BCC-CSM2-MR and BCC-CSM1.1m. As the NSIDC data we have are from 1979 to 2010, which are not long enough to meet our needs here, observation-based HadISST sea ice data, instead of NSIDC data, are plotted when available, where sea ice extent are computed from sea ice concentration. The Arctic sea-ice extent in BCC-CSM2-MR is slightly improved, in comparison to BCC-CSM1.1m. But the Antarctic minimum sea-ice extent in the new model is very small, almost a third of what observed. The old model had however a more realistic behavior for this regard. This discrepancy is related to too-warm temperatures simulated in BCC-CSM2-MR in the Southern Ocean, in particular in the Weddell Sea. The downward trend in the Arctic summer sea-ice extent is, however, better simulated in the new model than in the old one.

Figure 15 shows the seasonal cycle of sea ice extent (SIE) and thickness in the two Polar Regions in our models. Observations from the National Snow and Ice Data Center (NSIDC) and the European Centre for Medium-Range Weather Forecasts (ECMWF) are also plotted for the purpose of comparison. Observations from NSIDC show that Arctic sea ice cover reaches a minimum extent of 7.74×10^6 km^2 in September and rises to a maximum extent of 15.79×10^6 km^2 in March (Fig. 15a). The two models can both capture the seasonal variation and pattern, but large biases exist in magnitude, especially in boreal winter. As to Antarctic SIE, the ice cover undergoes a very large seasonal cycle, which is similar to observations. However, the SIE in BCC-CSM1.1m is too extensive throughout the year, particularly in southern hemisphere winter. Comparatively, the new model BCC-CSM2-MR simulates a relatively smaller seasonal cycle and reduced ice cover in all months which is closer to observations. As to ice thickness, the two models simulate a thinner ice cover compared to observations in all seasons for both Arctic and Antarctic. The most remarkable improvements of BCC-CSM2-MR appear in the boreal warm seasons, especially from June to September with thicker ice presented in the Arctic Ocean. Those improvements may be partly achieved with the new model physics such as schemes for turbulent flux over sea ice and ocean surfaces, cloud fraction, or atmospheric circulation improvements at high latitudes.

The Atlantic Meridional Overturning Circulation (AMOC) plays a significant role in driving the global climate variation (Caesar et al., 2018). AMOC consists of two primary overturning cells. In the upper cell, warm water flows northward in the upper 1000 m to supply the formation of the North Atlantic Deep Water (NADW), which returns southward in the depth range of approximately 1500 to 4000 m. In contrast, in the lower cell, the Antarctic Bottom Water (AABW) flows northward in the Atlantic basin beneath NADW. Figure 16 shows the time-averaged AMOC simulated by the two coupled model versions. The two main cells are well depicted. The lower branch of NADW is much deeper in BCC-CSM2-MR than in BCC-CSM1.1m, as indicated by the depth of the zero-contour line. Moreover, the central intensity of NADW in BCC-CSM2-MR is over 22.5 Sv about 2.5 Sv stronger than that in BCC-CSM1.1m, close to observation-based value (25 Sv in Talley et al., 2013).

4.7 Evaluation of models for their performance in East Asia

A good simulation of climate over East Asia is always a challenging issue for the climate modelling

679 community, as the region is under influences of complex topography (high Tibetan Plateau), and
680 atmospheric circulations from low latitudes (tropical monsoon circulation) and from higher latitudes.
681 Figure 17 plots a Taylor diagram to show models performance of main climate variables over East Asia
682 covering the region (100°-140°E, 20°-50°N). Both BCC-CSM1.1m (blue figures) and BCC-CSM2-MR
683 (red figures) are plotted for precipitation, sea-level pressure and variables of the atmospheric general
684 circulation. There is a clear and remarkable improvement from CMIP5 to CMIP6 in BCC models. The
685 amelioration is both in the spatial pattern correlation (radial lines) and in the ratio of standard deviations
686 (circles from the origin).
687 Figure 18 shows the 1980-2005 climatology of December-January-February and June-July-August
688 averaged precipitation over China and its surroundings. In boreal winter, GPCP precipitations show a
689 rain belt from Southeast China to Japan and another rain belt along the southwestern flank of the
690 Tibetan Plateau. In BCC-CSM1.1m the winter precipitation is too weak in Southeast China and too
691 strong near Japan, compared to GPCP observations. This rain belt in BCC-CSM2-MR obviously
692 spreads westward and is much closer to observations. The rain belt along the southwestern flank of the
693 Tibetan Plateau in BCC-CSM2-MR, however, gets too strong. In boreal summer, large dry biases over
694 East China are present in BCC-CSM1.1m. Those biases are reduced in BCC-CSM2-MR. The center of
695 precipitation around Japan is also well simulated in BCC-CSM2-MR.
696 The East Asian summer monsoon rainfall has a seasonal progression from south to north at the
697 beginning of summer and then a quick retreat to the south when the summer monsoon terminates (as
698 shown in Figure 19a). This phenomenon is strongly related to the fact that the East Asian monsoon
699 rainfall mainly takes place in the frontal zone between warm and humid air mass from the south, and
700 cold and dry air mass from the north. This seasonal migration is also accompanied with a meridional
701 movement of the Western North Pacific Subtropical High, an important atmospheric center of action
702 controlling the climate of the region. In Figure 19 (panels b and c), we compare the two models in terms
703 of seasonal migration of the monsoon rainfall. In the old model, rainfall was too weak. The new model
704 produces more precipitation. In terms of seasonal match, both models show a delay of the peak rainfall
705 by about one month, even longer in BCC-CSM2-MR.
706 Finally, let us examine the rainfall diurnal cycle in summer. Figure 20 shows the timing of the

rainfall diurnal cycle from observation and the two models. Main zones of nocturne rainfall can be recognized in the south flank of the Tibetan Plateau, in the Sichuan Basin in the east of the Tibetan Plateau, and in the north of Xinjiang in Central Asia. There is also a zone of nocturne rainfall in the low reach of the Yellow River. This is mainly under the influence of nocturne rainfall in the area of the Bohai Sea. Other regions over land experience diurnal rainfall peak in the afternoon after 16 hours local time. The diurnal cycle of rainfall was extensively studied in Jin et al. (2013) in terms of physics causing the diurnal cycle. But the good simulation of diurnal cycle is always a major challenge for climate modeling. We can see that it is not very well simulated in our old model and in East China the peak occurs in the mid and later night (0-4 am). But the improvement is quite spectacular in our new model with rainfall peak delayed in the afternoon. Such an improvement is due to the implementation of our new trigger scheme in convection parameterization.

5. Conclusions and discussion

This paper presents the main progress of BCC climate system models from CMIP5 to CMIP6 and focuses on the description of CMIP6 version BCC-CSM2-MR and CMIP5 version BCC-CSM1.1m especially on the model physics. Main updates in model physics include a modification of deep convection parameterization, a new scheme for cloud fraction, indirect effects of aerosols through clouds and precipitation, and the gravity wave drag generated by deep convection. Surface processes in BCC-AVIM have also been significantly improved for soil water freezing treatment, snow aging effect on surface albedo, and timing of vegetation leaf unfolding, growth, and withering. A four-stream radiation transfer within the vegetation canopy replaced the two-stream radiation transfer. There is a new treatment for rice paddy waters. New schemes for surface turbulent fluxes of momentum, heat and water at the interface of atmosphere and sea/sea ice are also used.

The evaluation of model performance in simulating present-day climatology is presented for main climate variables, such as, surface air temperature, precipitation, and atmospheric circulation for the globe and for East Asia. Emphasis is put on comparison between the CMIP5 and CMIP6 model versions (BCC-CSM2-MR versus BCC-CSM1.1m). The globally-averaged TOA net energy budget is 0.85 W • m^{-2} in BCC-CSM2-MR, and 0.98 W m^{-2} in BCC-CSM1.1m. Both versions have a very good energy equilibrium. Model biases of excessive cloud shortwave and longwave radiative forcings over

low latitudes in BCC-CSM1.1m are obviously reduced in BCC-CSM2-MR. When Taylor diagrams are used to compare the two models for spatial patterns of main climate variables such as 2-meter surface air temperature, precipitation, and atmospheric general circulation, BCC-CSM2-MR shows an overall improvement at both global scale and regional scale in East Asia. These improvements in BCC-CSM2-MR are believed to be achieved by the new scheme of cloud fraction and by the consideration of indirect effects of aerosol on clouds and precipitation. The cold tongue bias of SST in the equatorial Pacific in BCC-CSM1.1m still exists in BCC-CSM2-MR. BCC-CSM1.1m has a severe bias in sea ice extent (SIE) and thickness (Tan et al., 2015): too extensive in cold seasons and less extensive in warm seasons in both hemispheres. The most impressive improvements in BCC-CSM2-MR appear in the boreal warm seasons, especially from June to September with thicker ice presented in the Arctic Ocean. However, in the Southern Hemisphere, the sea ice extent and thickness in BCC-CSM2-MR become even smaller than those in its previous version. This is still an issue that needs to be addressed in our future work. There is another model bias of weak oceanic overturning circulation in BCC-CSM1.1m. This bias is reduced in the new version BCC-CSM2-MR, and the strength of AMOC is increased.

Further evaluations are performed on climate variabilities at different time scales, including long-term trend of global warming in the 20th century, QBO, MJO, and diurnal cycle of precipitation. The globally-averaged annual-mean surface air temperature from the historical simulation of BCC-CSM2-MR is much closer to HadCRUT4 observation than BCC-CSM1.1m, and the observed global warming hiatus or warming slowdown in the period from 1998 to 2013 is captured in some realization of BCC-CSM2-MR. With a higher vertical resolution and inclusion of the gravity wave drag generated by deep convection, the new version BCC-CSM2-MR is able to reproduce the stratospheric QBO, while QBO even does not exist in BCC-CSM1.1m. Further investigations on physical mechanisms controlling QBO simulation in BCC-CSM2-MR will be reported in future. MJO is a very important atmospheric oscillation at intra-seasonal scales and main features are reproduced and improved in BCC-CSM2-MR, but with intensity still weaker than its counterpart in observation. At interannual scale, BCC-CSM1.1m shows too-strong variations of Nino 3.4 SST index, but too-short and too-regular periodicity for ENSO. BCC-CSM2-MR shows weaker amplitude for Nino 3.4 SST index,

763 which is an improvement and closer to HadISST observations. The rainfall diurnal cycle in China has
764 strong regional variations with pronounced nocturne rainfalls in the Sichuan Basin and in north China
765 near the Bohai Sea and the coast. The diurnal rainfall generally peaks in the local time afternoon for
766 most other land regions. BCC-CSM2-MR shows a clear improvement of rainfall diurnal peaks
767 compared to the CMIP5 model (BCC-CSM1.1m). This improvement of rainfall diurnal variation is
768 strongly related to the modification of deep convection scheme.

769 Finally, we also evaluate the climate sensitivity to CO_2 increasing in the standard simulation of 1%
770 CO_2 increase per year (1pctCO2) and the 4xCO2 abrupt-change. The transient climate response in the
771 new CMIP6 model version BCC-CSM2-MR is lower than that in the previous CMIP5 model
772 BCC-CSM1.1m, while the equilibrium climate sensitivity ECS for BCC-CSM2-MR is slightly higher
773 than its counterpart in BCC-CSM1.1m.

774 From our model evaluations, we find that although basic feature of the QBO can be simulated in
775 BCC-CSM2-MR, the magnitude between westerly and easterly interchange is still too weak. We also
776 note that there are large biases of air temperature and winds in the stratosphere. Therefore, improvement
777 of the stratospheric temperature and circulation simulations is an important priority in the future
778 development of BCC models. In addition, sea ice simulation in the Antarctic region has large biases,
779 which need to be improved.

780 **6. Code and data availability**

781 Source codes of BCC models are freely available upon request addressed to Tongwen Wu
782 (twwu@cma.gov.cn). Model output of BCC models for both CMIP5 and CMIP6 simulations described
783 in this paper is distributed through the Earth System Grid Federation (ESGF) and freely accessible
784 through the ESGF data portals after registration. Details about ESGF are presented on the CMIP Panel
785 website at http://www.wcrp-climate.org/index.php/wgcm-cmip/about-cmip.

786

787 **Author contributions**

788 Tongwen Wu led the BCC-CSM development. Tongwen Wu and Xiaoge Xin designed the experiments
789 and carried them out. Tongwen Wu, Laurent Li, and Xiaohong Liu wrote the final document with
790 contributions from all other authors.

Acknowledgements

This work was supported by The National Key Research and Development Program of China (2016YFA0602100).

References

Albrecht, B.: Aerosols, cloud microphysics, and fractional cloudiness, Science, 245, 1227–1230, 1989.

Adler, R. F., Chang, A.: The Version 2 Global Precipitation Climatology Project (GPCP) Monthly Precipitation Analysis (1979-Present), J. Hydrometeor., 4, 1147–1167, 2003

Alexander, M. J., May, P. T., and Beres, J. H.: Gravity waves generated by convection in the Darwin area during the Darwin Area Wave Experiment, J. Geophys. Res., 109, D20S04, doi: 10.1029/2004JD004729, 2004.

Allen, M., Stott, P., Mitchell, J., Schnur, R., and Delworth, T.: Quantifying the uncertainty in forecasts of anthropogenic climate change, Nature, 407, 617-620, 2000.

Arora, V. K., and Boer, G. J.: A parameterization of leaf phenology for the terrestrial ecosystem component of climate models, Global Change Biology, 11, 39-59, doi:10.1111/j.1365-2486.2004.00890.x, 2005.

Andreas, E. L.: A theory for the scalar roughness and the scalar transfer coefficients over snow and sea ice, Bound.-Layer Meteor., 38, 159-184, 1987.

Andreas, E. L.: Parameterizing scalar transfer over snow and ice: A review, Journal of Hydrometeorology, 3, 417-432, 2002.

Andreas, E. L., Horst, T. W., Grachev, A. A., Persson, P. O. G., Fairall, C. W., and Guest, P. S.,and Jordan, R.E.: Parametrizing turbulent exchange over summer sea ice and the marginal ice zone, Quartely Journal of the Royal Meteorological Society, 136, 927-943, 2010a.

Andreas, E. L., Persson, P. G., Jordan, R. E., Horst, T.W., Guest, T.S., Grachev, A.A., and Fairall, C.W.: Parameterizing turbulent exchange over sea ice in winter, Journal of Hydrometeorology, 11, 87-104, 2010b.

Andrews, T., Gregory, J. M., Webb, M. J., and, K. E.: Forcing, feedbacks and climate sensitivity in CMIP5 coupled atmosphereocean climate models, Geophys. Res. Lett, 38, L09712, doi: 10.1029/2012GL051607, 2012.

Beres, J. H., Alexander, M. J., and Holton, J. R.: A method of specifying the gravity wave spectrum above convection based on latent heating properties and background wind, J. Atmos. Sci., 61, 324-337, 2004.

Boucher, O., Lohmann, U.: The sulphate-CCN-cloud albedo effect – a sensitivity study with two general circulation models, Tellus 47B, 281–300, 1995.

821 Caesar, L., Rahmstorf, S., Robinson, A., Feulner, G., Saba, V.: Observed fingerprint of a weakening Atlantic
822 Ocean overturning circulation, Nature, 556, 191-196, 2018.
823 Campin J.M., and Goosse, H.: Parameterization of density-driven downsloping flow for a coarse-resolution ocean
824 model in z-coordinate, Tellus, 51A, 412–430, 1999.
825 Cao M., and Woodward F. I.: Net primary and ecosystem production and carbon stocks of terrestrial ecosystems
826 and their responses to climate change, Global Change Biology, 4, 185-198, 1998.
827 Chen C., and Cotton, W. R.: The physics of the marine stratocumulus-capped mixed layer, J. Atmos. Sci., 44 (50),
828 2951–2977, 1987.
829 Chen A., Li, W. P., Li, W. J., and Liu, X.: An observational study of snow aging and the seasonal variation of
830 snow albedo by using data from Col de Porte, France. Chinese Science Bulletin, 59 (34), 4881-4889, 2014
831 Collins, W. D., Rasch, P.J., Boville, B.A., Hack, J. J., McCaa, J.R., Williamson, D. L., Kiehl, J. T., Briegleb, B.,
832 Bitz C., Lin S.J., Zhang, M.H., and Dai, Y.J.: Description of the NCAR community atmosphere model
833 (CAM3). Technical Report NCAR/TN-464 + STR, National Center for Atmospheric Research, Boulder,
834 Colorado, 226 pp, 2004.
835 Collins, W. J., Lamarque, J.–F., Schulz,M., Boucher, O., Eyring, V., Hegglin, M. I., Maycock, A., Myhre, G.,
836 Prather, M., Shindell, D., and Smith, S. J.: AerChemMIP: quantifying the effects of chemistry and aerosols
837 in CMIP6, Geosci. Model Dev., 10, 585–607, 2017.
838 Danabasoglu, G., and Co-authors: North Atlantic simulations in Coordinated Ocean-ice Reference
839 Experiments phase II (CORE-II). Part I: Mean States. Ocean Modelling, 73, 76-107, doi:
840 10.1016/j.ocemod.2013.10.005, 2014.
841 Dee, D.P., Uppala, S. M., Simmons, A. J., Berrisford, P., Poli, P., Kobayashi, S., Andrae, U., Balmaseda, M. A.,
842 Balsamo, G., Bauer, P., Bechtold, P., Beljaars, A. C. M., Berg L., Bidlot, J., Bormann, N., Delsol, C., Dragani,
843 R., Fuentes, M., Geer, A. J., Haimberger, L., Healy, S. B., Hersbach, H., Holm, E. V., Isaksen, L., Kallberg, P.,
844 Kohler, M., Matricardi, M., NcNally, A.P., Monge-Sanz, B. M., Morcrette, J.-J., Park, B.-K., Peubey, C.,
845 Rosnay, P., Tavolato, C., Thepaut, J.-N., and Vitart F.: The ERA-Interim reanalysis: configuration and
846 performance of the data assimilation system,Quart. J. R. Meteorol. Soc., 137, 553-597 (DOI:
847 10.1002/qj.828) , 2011。
848 Ding, Y. H., Liu, Y. M., Song, Y. J., Li, Q. Q.: Research and experiments of the dynamical model system for
849 short-term climate prediction, Climatic Environ. Res., 7(2), 236–246, 2002 (in Chinese).
850 Eyring, V., Bony, S., Meehl, G. A., Senior, C. A., Stevens, B., Stouffer, R. J., Taylor, K. E.: Overview of the

851 Coupled Model Intercomparison Project Phase 6 (CMIP6) experimental design and organization, Geosci.
852 Model Dev., 9, 1937–1958, 2016, 2017.
853 Fetterer, F., Knowles, K., Meier, W., Savoie, M.: Sea Ice Index, digital media, National Snow and Ice Data Center.
854 Boulder, CO., 2002.
855 Fyfe, J.C., Meehl, G.A., England, M.H., Mann, M. E. Santer, B. D., Flato, G. M., Hawkins, E., Gillett, N. P., Xie,
856 S.–P., Kosaka, Y., Swart, N. C.: Making sense of the early-2000s warming slowdown, Nat. Clim. Change 6,
857 224–228, 2016.
858 Griffies, S. M., Gnanadesikan, A., Dixon, K. W., Dunn e, J. P., Gerdes, R., Harrison, M. J., Rosati, A., Lin, J.,
859 Bonita, R., Samuels, L., Spelman, M. J., Winton, M., Zhang, R.J.: Formulation of an ocean model for
860 global climate simulations, Ocean Sci., 1, 45–79, 2005.
861 Gregory, J. M., Ingram, W. J., Palmer, M. A., Jones, G. S., Stott, P. A., Thorpe, R. B., Lowe, J. A., Johns, T. C.,
862 and Williams, K. D.: A new method for diagnosing radiative forcing and climate sensitivity, Geophys. Res.
863 Lett., 31, L03205, doi:10.1029/2003GL018747, 2004.
864 Gregory, J.M., Webb, M. J., and Taylor, K. E.: Forcing, feedbacks and climate sensitivity in CMIP5 coupled
865 atmosphere-ocean climate models, Geophys. Res. Lett., 39, L09712, doi:10.1029/2012GL051607, 2012.
866 Gent, P. R., Mcwilliams, J. C.: Isopycnal mixing in ocean circulation Models[J]. Journal of Physical
867 Oceanography, 20(1), 150–155, 1990.
868 Guenther, A. B., Jiang, X., Heald, C. L., Sakulyanontvittaya, T., Duhl, T., Emmons, L. K., and Wang, X.: The
869 Model of Emissions of Gases and Aerosols from Nature Version 2.1 (MEGAN2.1): An Extended and
870 Updated Framework for Modeling Biogenic Emissions, Geoscientific Model Development 5(6): 1471–1492,
871 2012.
872 Hack, J. J., Parameterization of moist convection in the National Center for Atmospheric Research Community
873 Climate Model (CCM2), J. Geophys. Res., 99, 5551–5568, 1994.
874 Haarsma, R. J., Roberts, M. J., Vidale, P. L., Senior, C. A., Bellucci, A., Bao, Q., Chang, P., Corti, S., Fuckar, N.
875 S., Guemas, V., Hardenberg, J. von, Hazeleger, W., Kodama, C., Koenigk, T., Leung, L. R., Lu, J., Luo, J. –J.,
876 Mao, J., Mizielinski, M. S., Mizuta, R. Nobre, P., Satoh, M., Scoccimarro, E., Semmler, T., Small, J., and
877 Storch, J.–S. von : High Resolution Model Intercomparison Project (HighResMIP v1.0) for CMIP6, Geosci.
878 Model Dev., 9, 4185–4208, doi:10.5194/gmd-9-4185-2016, 2016.
879 Holtslag, A. A. M., and Boville, B. A.: Local versus nonlocal boundary-layer diffusion in a global climate model,
880 J. Climate, 6, 1825–1842, 1993.

881 Huffman, G., Bolvin, D., Braithwaite, D., Hsu, K., Joyce, R., Xie, P.: Integrated Multi-satellitE Retrievals for
882 GPM (IMERG), version 4.4. NASA's Precipitation Processing Center, accessed 31 March, 2015,
883 ftp://arthurhou.pps.eosdis.nasa.gov/gpmdata/, 2014.
884 IPCC Climate Change: The Physical Science Basis (eds Stocker, T. F., Qin, D., Plattner, G.-K., Tignor, M., Allen,
885 S. K., Boschung, J., Nauels, A., Xia, Y., Bex V., and Midgley, P. M.) , Cambridge Univ. Press, Cambridge,
886 United Kingdom and New York, NY, USA, 2013.
887 Ji, J.: A climate-vegetation interaction model: Simulating physical and biological processes at the surface, Journal
888 of Biogeography, 22, 2063-2069, 1995.
889 Ji, J., Huang, M., and Li, K.: Prediction of carbon exchange between China terrestrial ecosystem and atmosphere
890 in 21st century, Sci. China Ser. D: Earth Sci., 51(6), 885-898, 2008.
891 Li, J. D., Wang, W.-C., Liao, H., and Chang, W. Y.: Past and future direct radiative forcing of nitrate aerosol in
892 East Asia, Theoretical and Applied Climatology, 121, 445-458, 2015.
893 Lu, B., Ren, H.-L.: Improving ENSO periodicity simulation by adjusting cumulus entrainment in BCC_CSMs,
894 Dynamics of Atmospheres and Oceans, 76, 127-140, 2016.
895 Jiang X., Waliser, D. E.Xavier, P.K., Petch, J., Klingaman, N. P., Woolnough, S.J., Guan, B., Bellon, G., Crueger,
896 T., DeMott, C., Hannay, C., Lin, H., Hu, W., Kim, D., Lappen, C., Lu, M.–M., Ma, H.-Y., Miyakawa, T.,
897 Ridout, J. A., Schubert, S.D., Scinocca, J., Seo, K.-H., Shindo, E., Song, X., Stan, C., Tseng, W.-L., Wang,
898 W., Wu, T., Wyser, K., Wu, X., Zhang, G. J., Zhu, H.: Exploring Key Processes of the Madden-Julian
899 Oscillation (MJO): A Joint WGNE MJO Task Force / GEWEX GASS Project on the Vertical Structure and
900 Diabatic Processes of the MJO – Part I. Climate Simulations, J. Geophys. Res. Atmos., 120, 4718–4748.
901 doi:10.1002/2014JD022375, 2015.
902 Jin, X., Wu, T., Li, L.: The quasi-stationary feature of nocturnal precipitation in the Sichuan Basin and the role of
903 the Tibetan Plateau, Climate Dynamics, 41: 977-994. DOI: 10.1007/s00382-012-1521-y, 2013.
904 Jones, C.D., Arora, V., Friedlingstein, P., Bopp, L., Brovkin, V., Dunne, J., Graven, H., Hoffman, F., Ilyina, T.,
905 John, J. G., Jung, M., Kawamiya, M., Koven, C., Pongratz, J., Raddatz, T., Randerson, J. T., and Zaehle, S.:
906 C4MIP – The Coupled Climate–Carbon Cycle Model Intercomparison Project: experimental protocol for
907 CMIP6, Geosci. Model Dev., 9, 2853–2880, doi:10.5194/gmd-9-2853-2016, 2016.
908 Klein, S. A., and Hartmann, D. L.: The seasonal cycle of low stratiform clouds, J. Climate, 6, 1587–1606, 1993.
909 Kristjánsson, J. E., Edwards, J. M., Mitchell, D. L.: Impact of a new scheme for optical properties of ice crystals
910 on climates of two GCMs, J. Geophys. Res., 105(D8), 10063–10079, doi:10.1029/2000JD900015, 2000.

911 Lamarque, J.-F., Emmons, L. K., Hess, P. G., Kinnison, D. E., Tilmes, S., Vitt, F., Heald, C. L., Holland, E. A.,
912 Lauritzen, P. H., Neu, J., Orlando, J. J., Rasch, P. J., and Tyndall, G. K.: CAM-chem: description and
913 evaluation of interactive atmospheric chemistry in the Community Earth System Model, Geosci Model Dev,
914 5, 369-411, 2012.
915 Large, W. G., McWilliams, J. C., and Doney, S. C.: Oceanic vertical mixing: A review and a model with a
916 nonlocal boundary layer parameterization, Rev. Geophys., 32, 363-403, 1994.
917 Liu, Y., and Daum, P. H.: Indirect warming effect from dispersion forcing, Nature, 419, 580-581, 2002.
918 Liou, K. N.: An Introduction to Atmospheric Radiation, China Meteorological Press, 313-327 (in Chinese), 2004.
919 Loeb, N.G., Lyman, J.M., Johnson, G.C,, Allan, R.P., Doelling, D.R., Wong, T., Soden, B.J., and Stephens, G.L.:
920 Observed changes in top-of-the-atmosphere radiation and upper-ocean heating consistent within uncertainty,
921 Nature Geosciences, DOI 10.1038/NGE, 2012.
922 Lu, Y., Zhou, M., and Wu, T.: Validation of parameterizations for the surface turbulent fluxes over sea ice with
923 CHINARE 2010 and SHEBA data, Polar Research, 32, 20818, http://dx.doi.org/10.3402/polar.v32i0.20818,
924 2013.
925 Meehl, G.A., Boer, G.J., Covey, C., Latif, M., Stouffer, R.J.: Intercomparison makes for a better climate model.
926 Eos, Trans.Amer.Geophys.Union, 78, 445--451, doi:10.1029/97EO00276.
927 Medhaug, I., Martin, B. S., Erich, M. F., and Knutti, R.: Reconciling controversies about the ‘global warming
928 hiatus’, Nature, 545, 41–47, 2017.
929 Morice, C, P., Kennedy, J. J., Rayner, N.A., and Jones, P.D.: Quantifying uncertainties in global and regional
930 temperature change using an ensemble of observational estimates: The HadCRUT4 data set, J. Geophys. Res.
931 117, D08101, 2012.
932 Martin, G.M., Johnson, D.W., and Spice, A.: The measurement and parameterisation of effective radius of
933 droplets in warm stratocumulus clouds, J. Atmos. Sci., 51, 1823–1842, 1994.
934 McFarlane, N. A.: The effect of orographically excited gravity wave drag on the general circulation of the lower
935 stratosphere and troposphere, J. Atmos. Sci., 44, 1775-1800, 1987.
936 Oleson, K. W., Lawrence, D. M. and Dai, Y. J.: Technical description of the Community Land Model (CLM),
937 NCAR Technical Note NCAR/TN-461+STR, 2004.
938 Pontikis, C.A., and Hicks, E.; Contribution to the cloud droplet effective radius parameterization, Geophys. Res.
939 Lett. 19, 2227–2230, 1992.
940 Peng, Y., and Lohmann, U.: Sensitivity study of the spectral dispersion of the cloud droplet size distribution on

941 the indirect aerosol effect, Geophys. Res. Lett., 30(10), 1507, doi:10.1029/2003GL017192, 2003.
942 Quaas J, Boucher O, and Lohmann U: Constraining the total aerosol indirect effect in the LMDZ and ECHAM4
943 GCMs using MODIS satellite data. Atmos Chem Phys 6,947-955, 2006
944 Rasch, P. J., and Kristj ánsson, J. E.: A comparison of the CCM3 model climate using diagnosed and predicted
945 condensate parameterizations, J. Climate, 11, 1587-1614, 1998.
946 Rahmstorf, S.: A fast and complete convection scheme for ocean models, Ocean Modelling, 101, 9–11, 1993.
947 Rayner, N. A., Parker, D. E., Horton, E. B., Folland, C., Alexander, L., Rowell, D., Kent, E., and Kaplan, A.:
948 Global analyses of sea surface temperature, sea ice, and night marine air temperature since the late
949 nineteenth century, Journal of Geophysical Research, 108(D14), 4407, doi:10.1029/2002JD002670, 2003.
950 Richter, J. H., Sassi, F., and Garcia, R. R.: Toward a physically based gravity wave source parameterization in a
951 general circulation model, J. Atmos. Sci., 67, 136--156, 2010.
952 Sweeney, C., Gnanadesikan, A., Griffies, S. M., Harrison, M., Rosati, A., Samuels, B.: Impacts of shortwave
953 penetration depth on large-scale ocean circulation and heat transport, Journal of Physical Oceanography 35,
954 1103–1119, 2005.
955 Stevens, B., Fiedler, S., Kinne, S., Peters, K., Rast, S., Musse, J., Smith, S.J., and Mauritsen, T.: MACv2-SP: a
956 parameterization of anthropogenic aerosol optical properties and an associated Twomey effect for use in
957 CMIP6, Geos.Mod.Dev.,10, 433-452, 2017.
958 Talley, L.D.: Closure of the global overturning circulation through the Indian, Pacific, and Southern Oceans:
959 Schematics and transports, Oceanography, 26, 80–97, 2013.
960 Tan, H.H., Zhang, L.J., Chu, M., Wu, T.W., Qiu, B., and Li, J.L.: An analysis of simulated global sea ice extent,
961 thickness, and causes of error with the BCC_CSM model. Chinese Journal of Atmospheric Sciences (in
962 Chinese), 39 (1): 197−209, 2015.
963 Taylor, K. E., Stouffer, R. J., and Meehl, G. A.: An Overview of Cmip5 and the Experiment Design, B. Am.
964 Meteorol. Soc., 93, 485–498, 2012.
965 Tietsche, S., Balmaseda, M., Zuo, H., Mogensen, K.: Arctic sea ice in the ECMWF MyOcean2 ocean reanalysis
966 ORAP5. Tech Rep 737, European Center for Medium-Range Weather Forecasts, Reading, UK, 2014.
967 Wielicki, B.A., Barkstrom, B. R., Harrison, E. F., Lee, R. B., Smith, G. L., and Cooper, J. E.: Clouds and the
968 earth's radiant energy system (CERES): an earth observing system experiment, Bull. Am. Meteorol. Soc., 77,
969 853–868, 1996.
970 Winton, M.: A reformulated three-layer sea ice model, J. Atmo.Oceanic Technol., 17, 525–531, 2000.

971 Wu, T., Song, L., Li, W., Wang, Z., Zhang, H., Xin, X., Zhang, Y., Zhang, L., Li, J., Wu, F., Liu, Y., Zhang, F., Shi,
972 X., Chu, M., Zhang, J., Fang, Y., Wang, F., Lu,Y., Liu, X., Wei, M., Liu, Q., Zhou, W., Dong, M., Zhao, Q., Ji,
973 J., Li, L., and Zhou, M.: An overview of BCC climate system model development and application for
974 climate change studies, J. Meteor. Res., 28(1), 34-56, 2014.
975 Wu, T., Li, W., Ji, J., Xin, X., Li, L., Wang, Z., Zhang, Y., Li, J., Zhang, F., Wei, M., Shi, X., Wu, F., Zhang, L.,
976 Chu, M., Jie, W., Liu, Y.,Wang, F., Liu, X., Li, Q., Dong, M., Liang, X., Gao, Y., and Zhang, J.: Global
977 carbon budgets simulated by the Beijing climate center climate system model for the last century, J Geophys
978 Res Atmos, 118, 4326-4347. doi: 10.1002/jgrd.50320, 2013.
979 Wu, T.: A Mass-Flux Cumulus Parameterization Scheme for Large-scale Models: Description and Test with
980 Observations, Clim. Dyn., 38:725–744, DOI: 10.1007/ s00382-011-0995-3, 2012.
981 Wu, T., Yu, R., Zhang, F., Wang, Z., Dong, M., Wang, L., Jin, X., Chen, D.L., and Li, L.：The Beijing Climate
982 Center atmospheric general circulation model: description and its performance for the present-day climate,
983 Climate Dynamics, 34, 123-147, DOI 10.1007/s00382-008-0487-2, 2010.
984 Wu, T., Yu, R., and Zhang, F.: A modified dynamic framework for atmospheric spectral model and its application,
985 J. Atmos.Sci., 65, 2235-2253, 2008
986 Wu, T., and Wu, G.: An empirical formula to compute snow cover fraction in GCMs, Adv.Atmos.Sci., 21,
987 529-535, 2004.
988 Xia, K., Luo, Y., and Li, W. P.: Simulation of freezing and melting of soil on the northeast Tibetan Plateau.
989 Chinese Sci. Bull., 56, 1-4, doi: 10.1007/s11434-011-4542-8, 2011.
990 Xin, X., Wu, T., and Zhang, J.: Introduction of CMIP5 experiments carried out with the climate system models of
991 Beijing Climate Center, Adv. Clim. Change Res., 4(1), 41-49，doi: 10.3724/SP.J.1248.2013.041, 2013.
992 Xu, K. M., and Krueger, S. K.: Evaluation of cloudiness parameterizations using a cumulus ensemble model,
993 Mon. Wea. Rev., 119, 342–367, 1991.
994 Xu, L., and Penner, J.E.: Global simulations of nitrate and ammonium aerosols and their radiative effects, Atmos.
995 Chem. Phys., 12, 9479-9504, 2012.
996 Zeng, X., Zhao, M., and Dickinson, R. E.: Intercomparison of bulk aerodynamic algorithms for the computation
997 of sea surface fluxes using TOGA COARE and TAO data, J. Climate, 11, 2628-2644, 1998.
998 Zeng, X., Zhang, Q., Johnson, D., and Tao, W.-K.: Parameterization of wind gustiness for the computation of
999 ocean surface fluxes at different spatial scales, Monthly Weather Review, 130, 2125-2133, 2002.
1000 Zhang, G.J.: Convective quasi-equilibrium in midlatitude continental environment and its effect on convective

parameterization. J Geophys Res 107(D14), doi:10.1029/2001JD001005, 2002.

Zhang, M., Lin, W., Bretherton, C. S., Hack, J. J., and Rasch, P. J.: A modified formulation of fractional stratiform condensation rate in the NCAR community atmospheric model CAM2, J. Geophys. Res., 108 (D1), 2003.

Zhang, Y., Gao, Z., Li, D., Li, Y., Zhang, N., Zhao, X., and Chen, J.: On the computation of planetary boundary-layer height using the bulk Richardson number method, Geosci. Model Dev., 7, 2599–2611, 2014.

Zhou, W.Y., Luo, Y., Li, W.P., Shi, X.L., and Zhang, Y: Comparative studies of different radiation schemes within vegetation in land model, Chinese Science Bulletin, 63, 10.1360/N972018-00398, 2018.

Table 1. BCC models for CMIP5 and CMIP6

Model versions	Atmosphere	Atmos Chemistry and Aerosol	Land Surface	Ocean	Sea Ice
BCC-CSM1.1 in CMIP5 (Wu et al., 2013)	BCC-AGCM2.1 (1) T42，26 layers (2) Top at 2.917 hPa	(1) Prescribed aerosols (2) No atmospheric chemistry (3) Global carbon budget without spatial distribution	BCC-AVIM1.0	MOM4-L40v1 (1) Tri-polar: 0.3 to 1 deg latitude x 1 deg longitude, and 40 layers (2) Oceanic carbon cycle based on OCMIP2	SISv1
BCC-CSM1.1m in CMIP5 (Wu et al., 2013)	BCC-AGCM2.2 (1) T106，26 layers (2) Top at 2.917 hPa	Same as BCC-CSM1.1	BCC-AVIM1.0	MOM4-L40v2	SISv2
BCC-CSM2-MR In CMIP6	BCC-AGCM3-MR (1) T106，46 layers (2) Top at 1.459 hPa	(1) Prescribed aerosols (2) No atmospheric chemistry (3) Prognostic spatial CO_2 in the atmosphere	BCC-AVIM2.0	MOM4-L40v2	SISv2
BCC-CSM2-HR In CMIP6	BCC-AGCM3-HR (1) T266，56 layers (2) Top at 0.092 hPa	(1) Prescribed aerosols (2) No atmospheric chemistry	BCC-AVIM2.0	MOM4-L40v2	SISv2
BCC-ESM1 In CMIP6	BCC-AGCM3-Chem (1) T42，26 layers (2) Top at 2.917 hPa	(1) Prognostic aerosols (2) MOZART2 atmospheric chemistry	BCC-AVIM2.0	MOM4-L40v2	SISv2

Table 2. Main physics schemes in atmospheric components (BCC-AGCM) of BCC-CSM versions for CMIP5 and CMIP6

	BCC-AGCM2 for CMIP5	**BCC-AGCM3 for CMIP6**
Deep convection	The cumulus convection parameterization scheme (Wu, 2012)	A modified Wu'2012 scheme described in this work
Shallow/Middle Tropospheric Moist Convection	Hack (1994)	Hack (1994)
Cloud macrophysics	Cloud fraction diagnosed from updraft mass flux and relative humidity (Collins et al., 2004)	A new scheme to diagnose cloud fraction described in this work
Cloud microphysics	Modified scheme of Rasch and Kristj ́ansson (1998) by Zhang et al. (2003). No aerosol indirect effects	Modified scheme of Rasch and Kristj ́ansson (1998) by Zhang et al. (2003), but included the aerosol indirect effects in which liquid cloud droplet number concentration is diagnosed using the aerosols masses.
gravity wave drag	Gravity wave drag only generated by orography (Mcfarlane 1987)	Gravity wave drag generated by both orography (Mcfarlane 1987) and convection (Beres et al., 2004) using tuned parameters related to model resolutions.
Radiative transfer	Radiative transfer scheme used in CAM3 (Collins et al., 2004) with no aerosol indirect effects, and cloud drop effective radius for clouds is only function of temperature and has a distinct difference between maritime, polar, and continental for warm clouds.	Radiative transfer scheme used in CAM3 (Collins et al., 2004), but including the aerosol indirect effects, and the effective radius of the cloud drop for liquid clouds is diagnosed using liquid cloud droplet number concentration.
Boundary Layer	ABL parameterization [Holtslag and Boville, 1993]	ABL parameterization [Holtslag and Boville, 1993], but modified PBL height computation referred to Zhang et al. (2014)

Table 3. Main physics schemes in BCC-AVIM versions

BCC-AVIM1.0 in CMIP5	BCC-AVIM2.0 in CMIP6
◆ Soil-Vegetation-Atmosphere Transfer module ◆ Multi-layer snow-soil scheme (same as NCAR CLM3) ◆ Snow Cover Fraction scheme (sub-grid topography) ◆ Vegetation growth module ◆ Soil carbon decomposition module ◆ Land use change module (variable crop planting area)	◆ Modified freeze-thaw scheme for soil water (below 0 degree and dependent on soil & water) (Xia et al., 2011) ◆ Improved parameterization of snow surface albedo (Chen et al., 2014) and snow cover fraction (Wu and Wu, 2004) ◆ Four-stream radiation transfer through vegetation canopy (Zhou et al., 2018) ◆ A vegetation phenology similar to Canadian Terrestrial Ecosystem Model (Arora and Boer, 2005) ◆ Parameterized rice paddy scheme ◆ land VOC module (Guenther et al., 2012)

Table 4. Energy balance and cloud radiative forcing at the top-of-atmosphere (TOA) in the model with contrast to CERES/EBAF and CERES observations. Units: $W \cdot m^{-2}$.

	BCC-CSM2-MR (CMIP6)	BCC-CSM1.1m (CMIP5)	CERES/EBAF (OBS)	CERES (OBS)
Net energy at TOA	0.85	0.98	0.81	5.73
TOA outgoing longwave radiative flux	239.15	236.10	239.72	238.95
TOA incoming shortwave Radiation	340.46	341.70	340.18	341.47
TOA net shortwave radiative flux	239.09	235.96	240.53	244.68
TOA outgoing longwave radiative flux in clear sky	265.02	265.58	265.80	266.87
TOA net shortwave radiative flux in clear sky	288.67	288.71	287.68	294.69
Shortwave cloud radiative forcing	-49.55	-52.71	-47.16	-48.58
Longwave cloud radiative forcing	25.87	29.48	26.07	27.19

Notes: The model data are the mean of 1986 to 2005, while the available observation data are for 2003–2014.

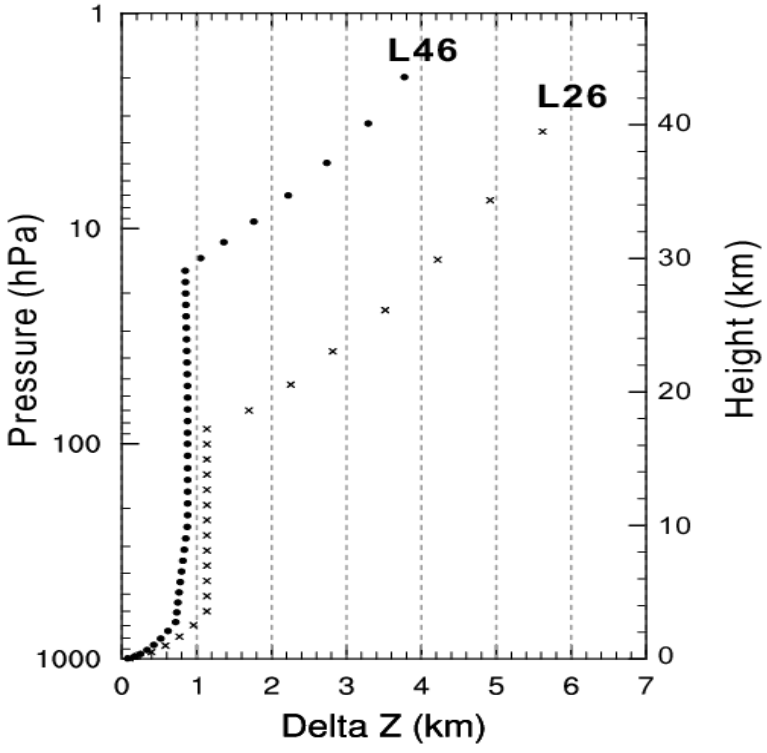

Figure 1. The profiles of layer thickness against the height for 26 vertical layers of the atmosphere in BCC-CSM-1.1m and 46 vertical layers in BCC-CSM2-MR.

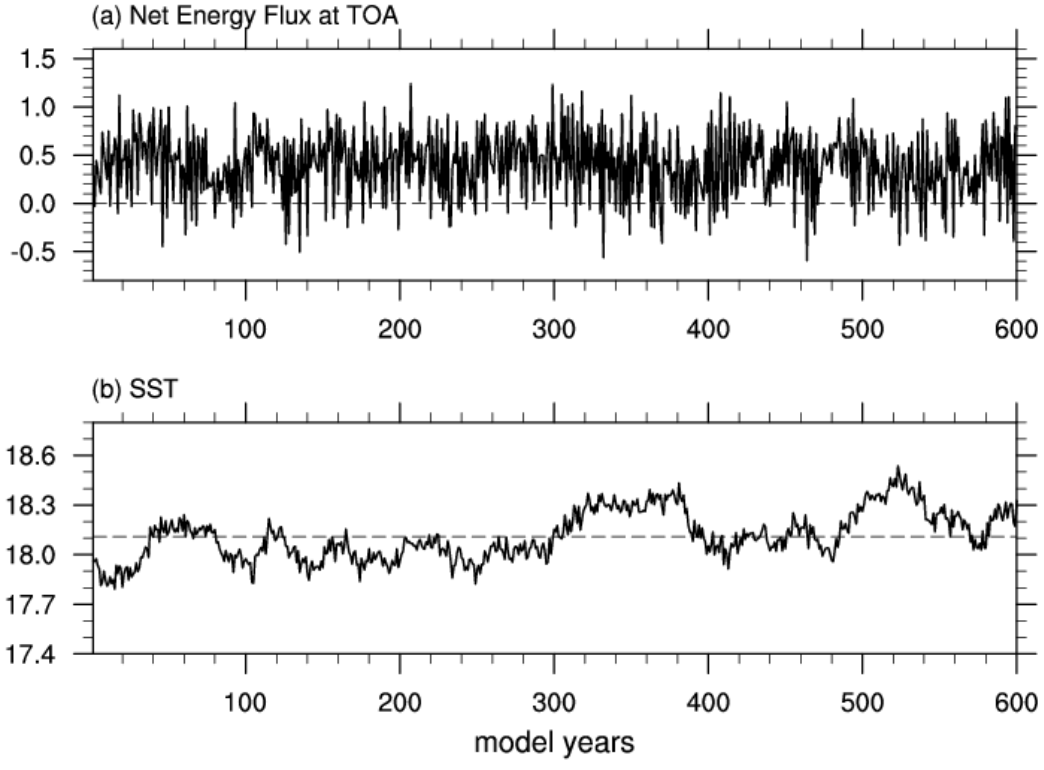

Figure 2. The time series of (a) global mean net energy flux at top of the atmosphere ($W \cdot m^{-2}$) and (b) global sea surface temperature for the 600 years of piControl simulations.

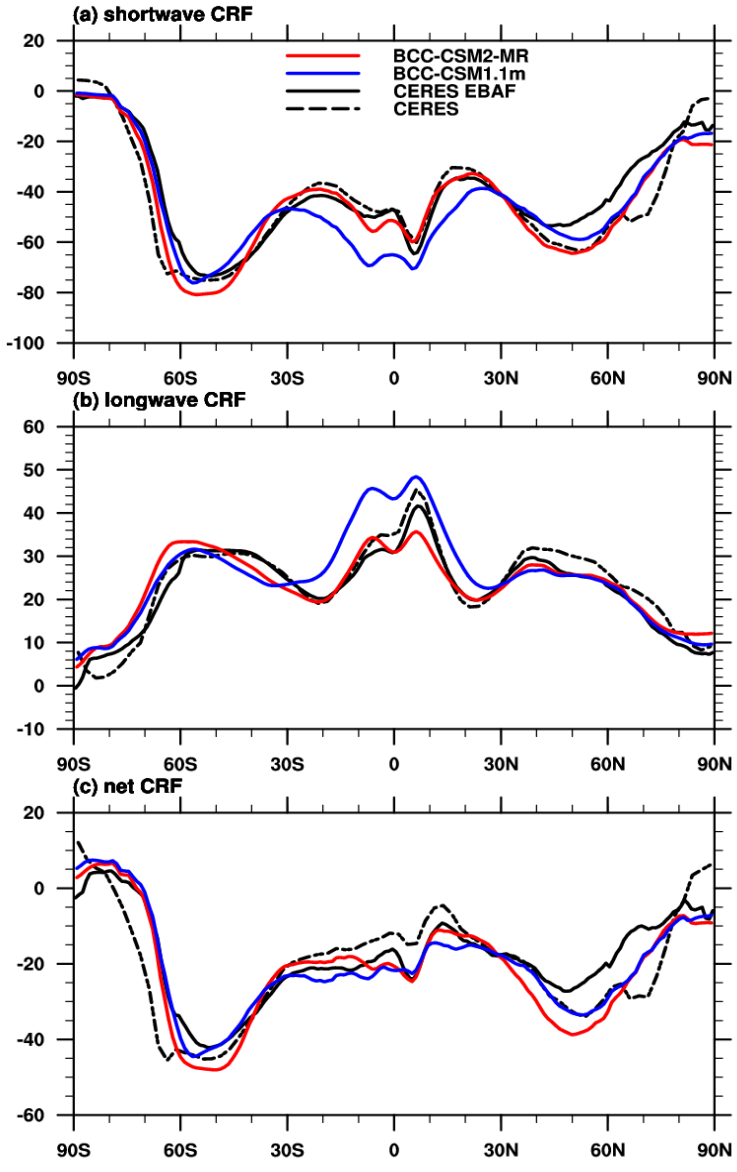

Figure 3. Zonal averages of the cloud radiative forcing from the BCC CMIP5 and CMIP6 models and observations (in W m^{-2}; top row: shortwave effect; middle row: longwave effect; bottom row: net effect). Model results are for the period 1986–2005, while the available CERES ES-4 and CERES EBAF 2.6 data set are for 2003–2014.

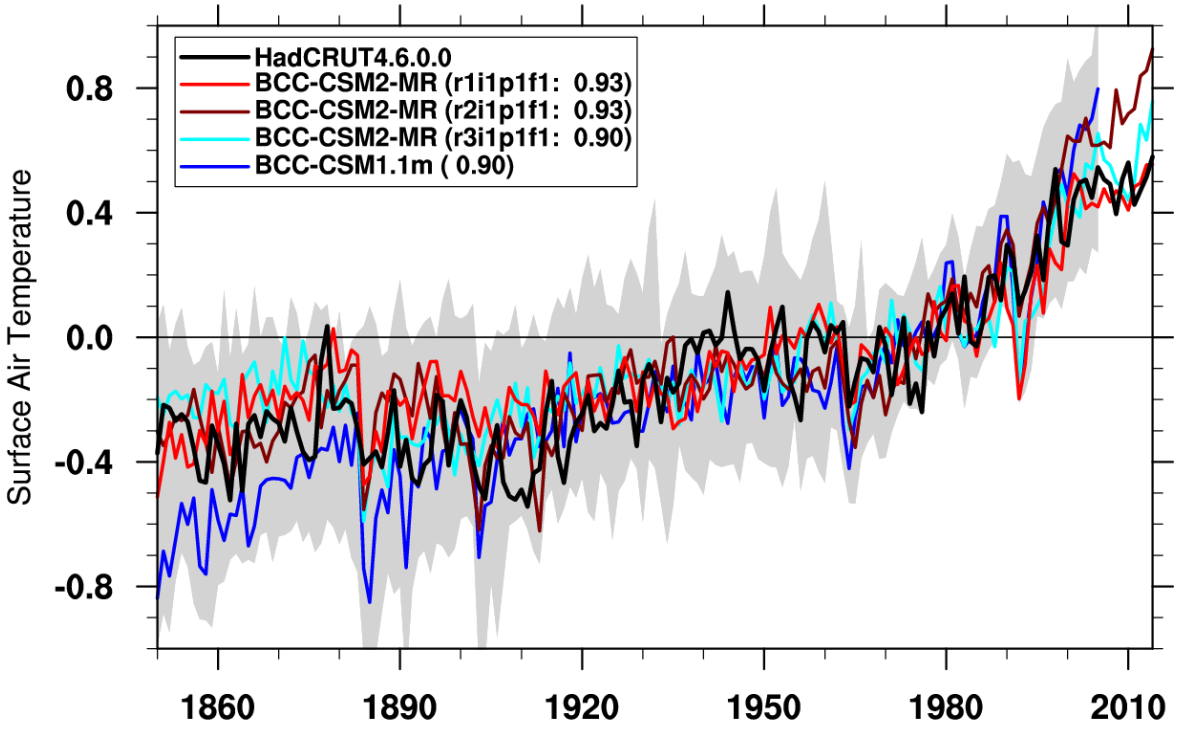

Figure 4. Time series of anomalies in the global (60 ℃S to 60 ℃N) mean surface air temperature from 1850 to 2014. The reference climate to deduce anomalies is for each individual curve from 1961 to 1990. Three lines labeled BCC-CSM2-MR denote three members of historical simulations from different initial state of the piControl simulation. The numbers in the bracket denote the correlation coefficient of 11-year smoothed BCC model data with the HadCRUT4.6.0.0 (Morice et al., 2012) observation. Gray shaded area shows the spread of 36 CMIP5 models data.

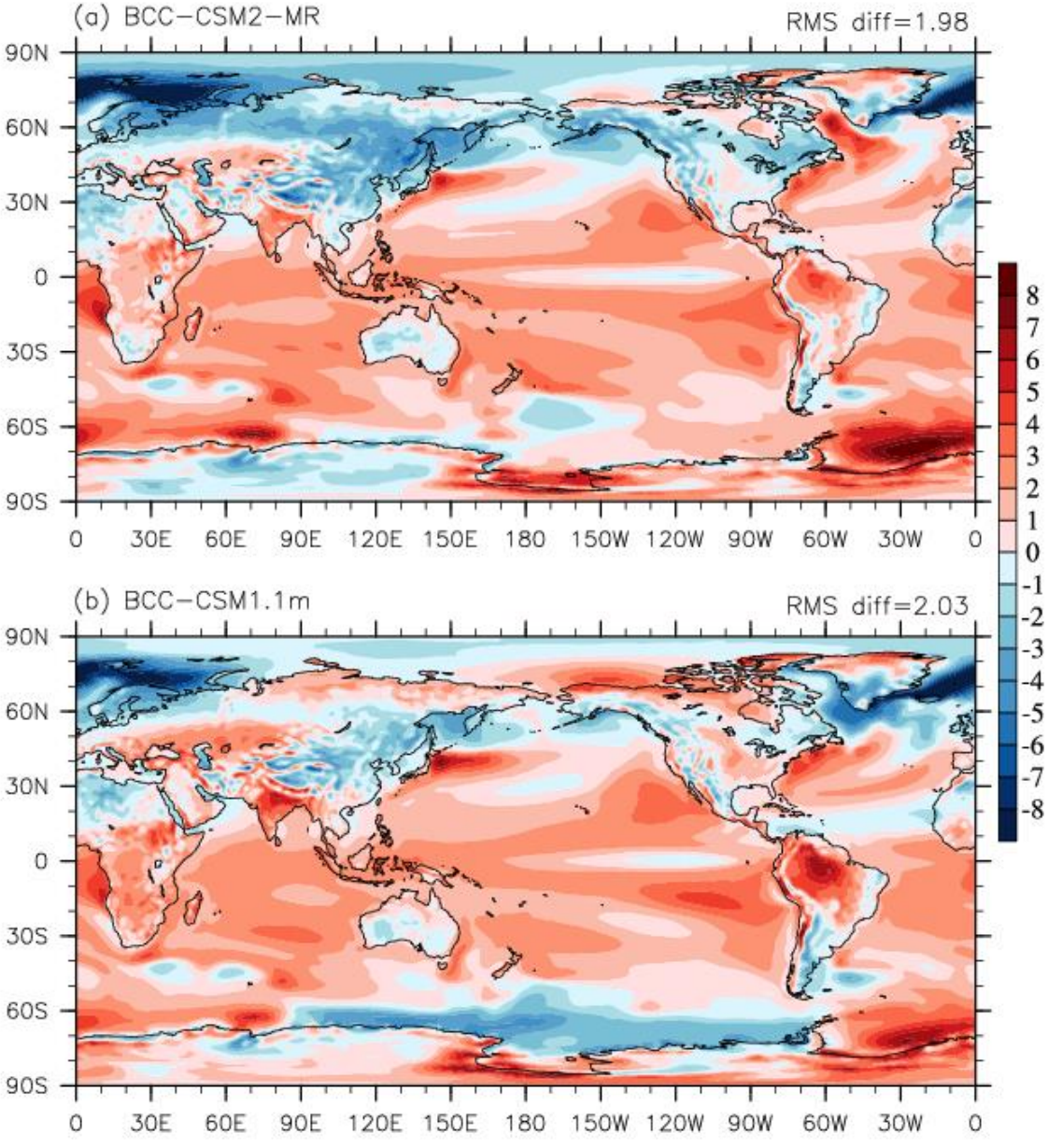

Figure 5. Annual-mean surface (2 meter) air temperature biases (℃) of (a) BCC-CSM2-MR and (b) BCC-CSM1.1m simulations with contrast to the reanalysis ERA-Interim for the period of 1986 to 2005.

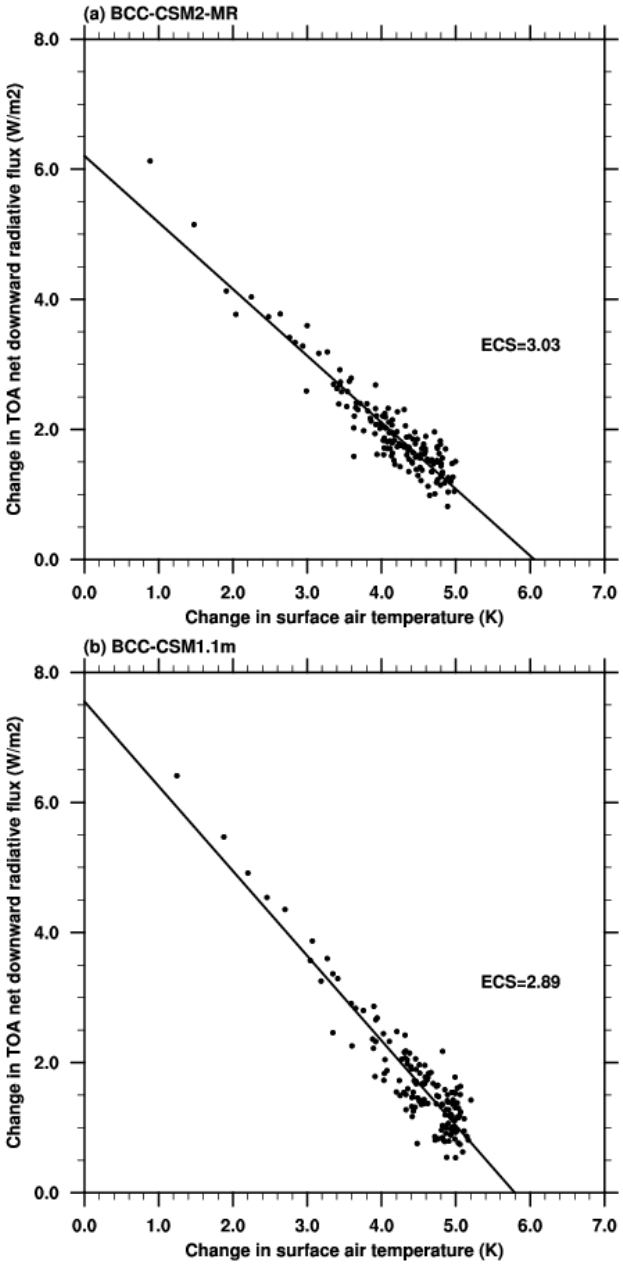

Figure 6. Relationships between the change in net top-of-atmosphere radiative flux and global-mean surface air temperature change simulated with an abrupt 4xCO_2 increase relative to the pre-industrial control run.

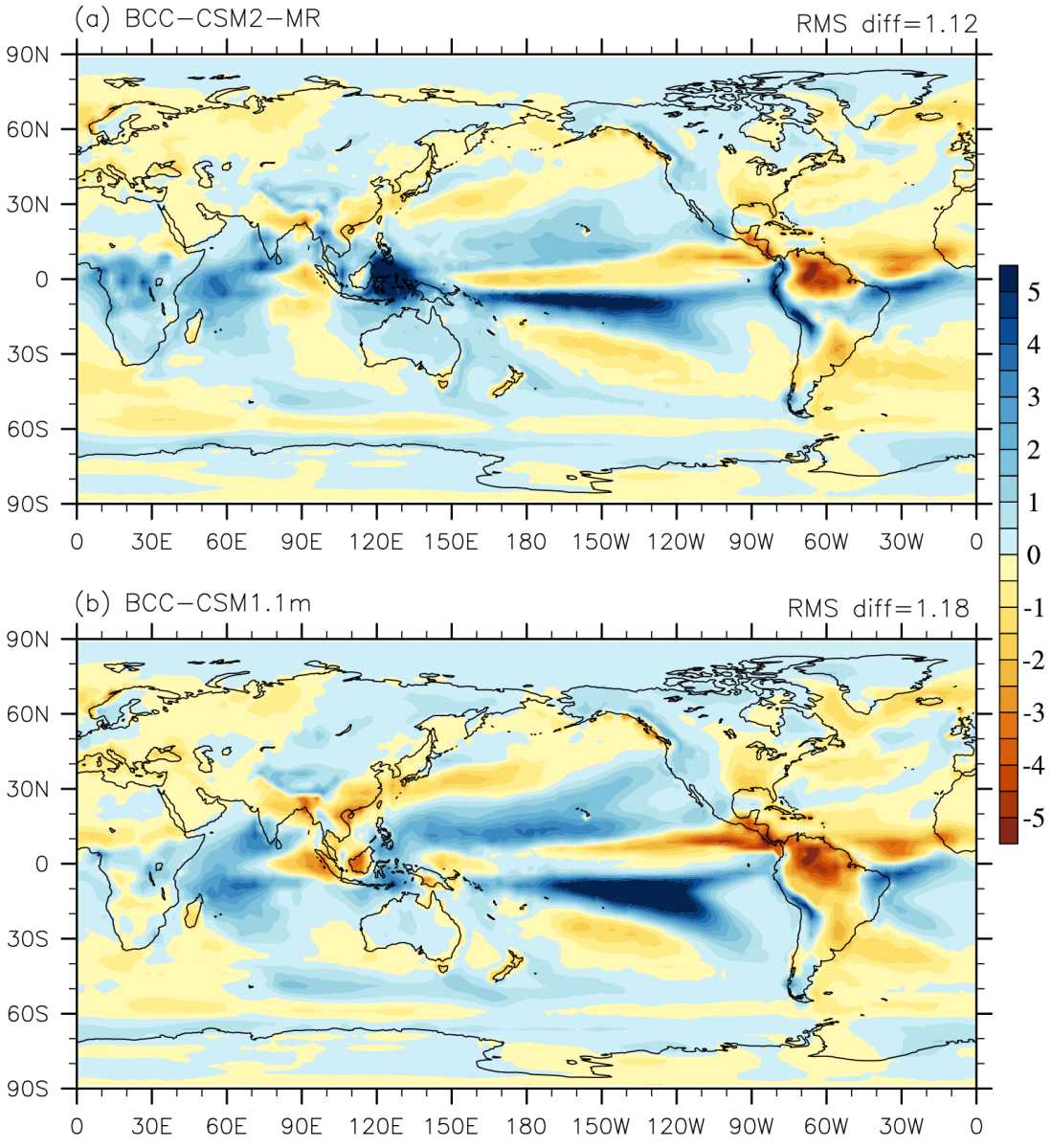

Figure 7. Annual-mean precipitation rate biases (mm day^{-1}) of (a) BCC-CSM2-MR and (b) BCC-CSM1.1m simulations with contrast to 1986-2005 precipitation analyses from the Global Precipitation Climatology Project (Adler et al., 2003)

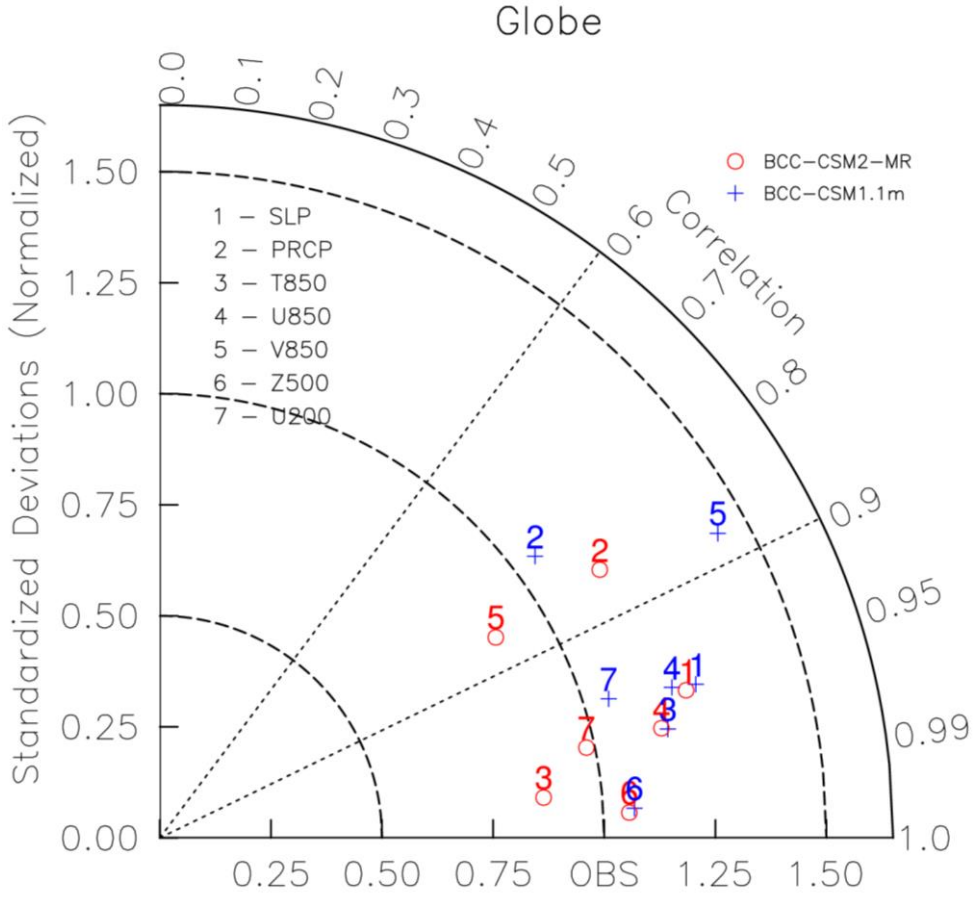

Figure 8. Taylor diagram for the global climatology (1980–2005) of sea level pressure (SLP), precipitation (PRCP), temperature at 850 hPa (T850), zonal wind at 850 hPa (U850), longitudinal wind at 850 hPa (V850), geopotential height at 500 hPa (Z500), and zonal wind at 200 hPa (U200). The radial coordinate shows the standard deviation of the spatial pattern, normalized by the observed standard deviation. The azimuthal variable shows the correlation of the modelled spatial pattern with the observed spatial pattern. Analysis is for the whole globe. The reference dataset is ERA-Interim except the precipitation from Global Precipitation Climatology Project dataset. The model results of BCC-CSM2-MR and BCC-CSM1.1m are the mean for 1980 to 2000. Blue crosses are for BCC-CSM1.1m and circles for BCC-CSM2-MR.

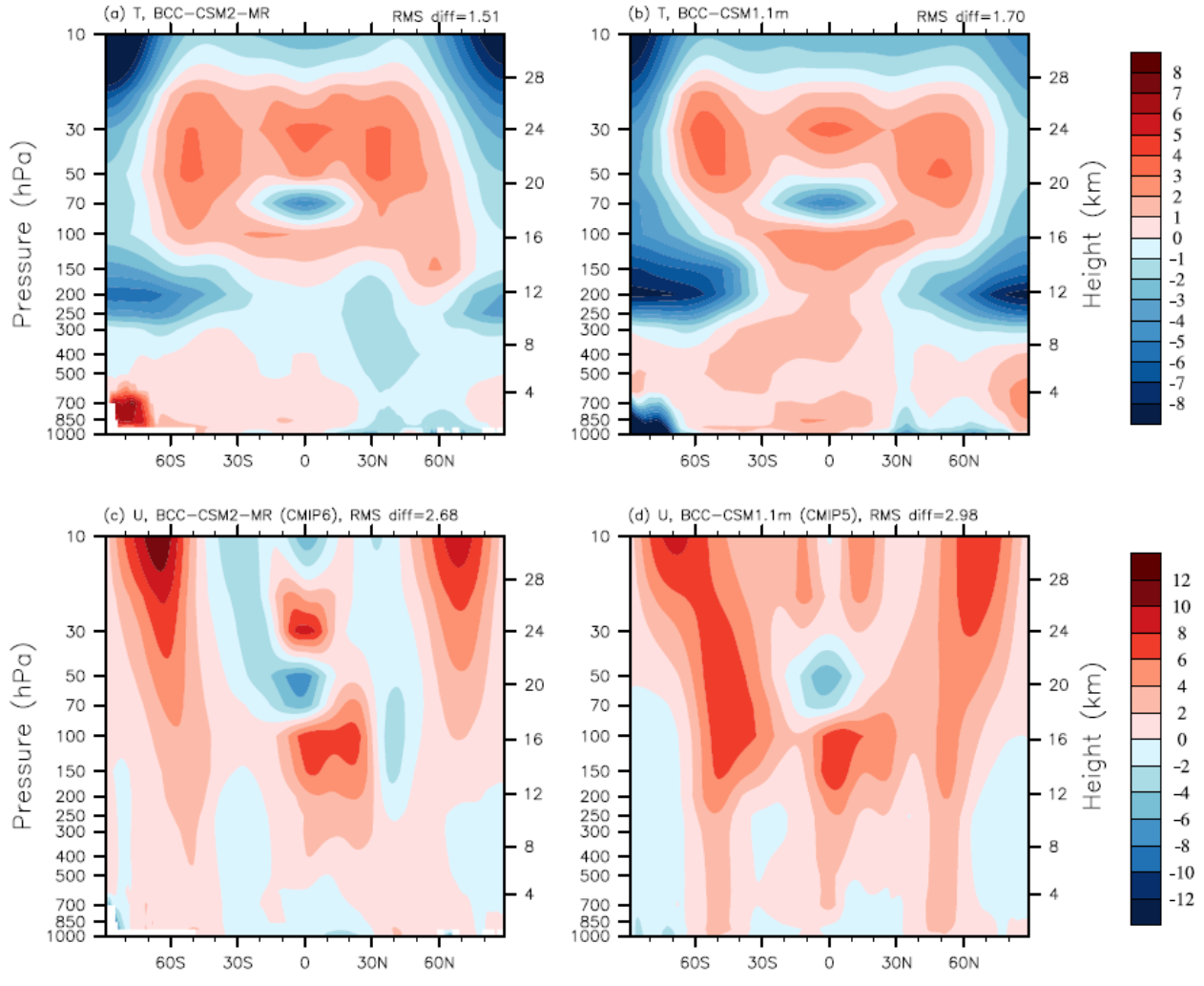

Figure 9. Pressure-latitude sections of annual mean temperature (top panels, K) and zonal wind (bottom, m s^{-1}) biases for BCC-CSM2-MR (left) and BCC-CSM1.1m (right), with respect to the reanalysis ERA-Interim for the period of 1986 to 2005.

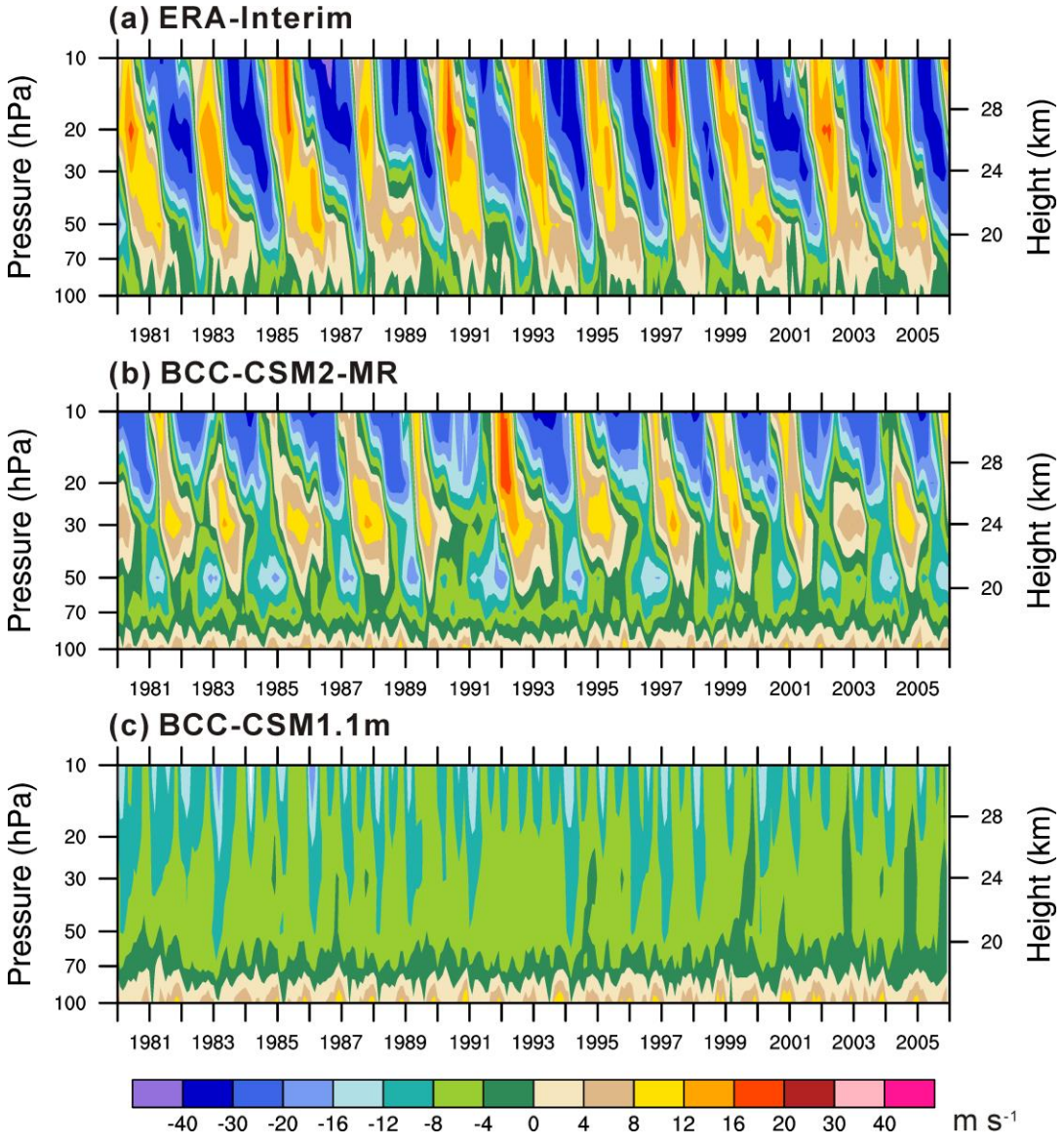

Figure 10. Tropical zonal winds (m s^{-1}) between 5 ℃S and 5 ℃N in the lower stratosphere from 1980 to 2005 for (a) ERA-Interim reanalysis, (b) BCC-CSM2-MR, and (c) BCC-CSM1.1m.

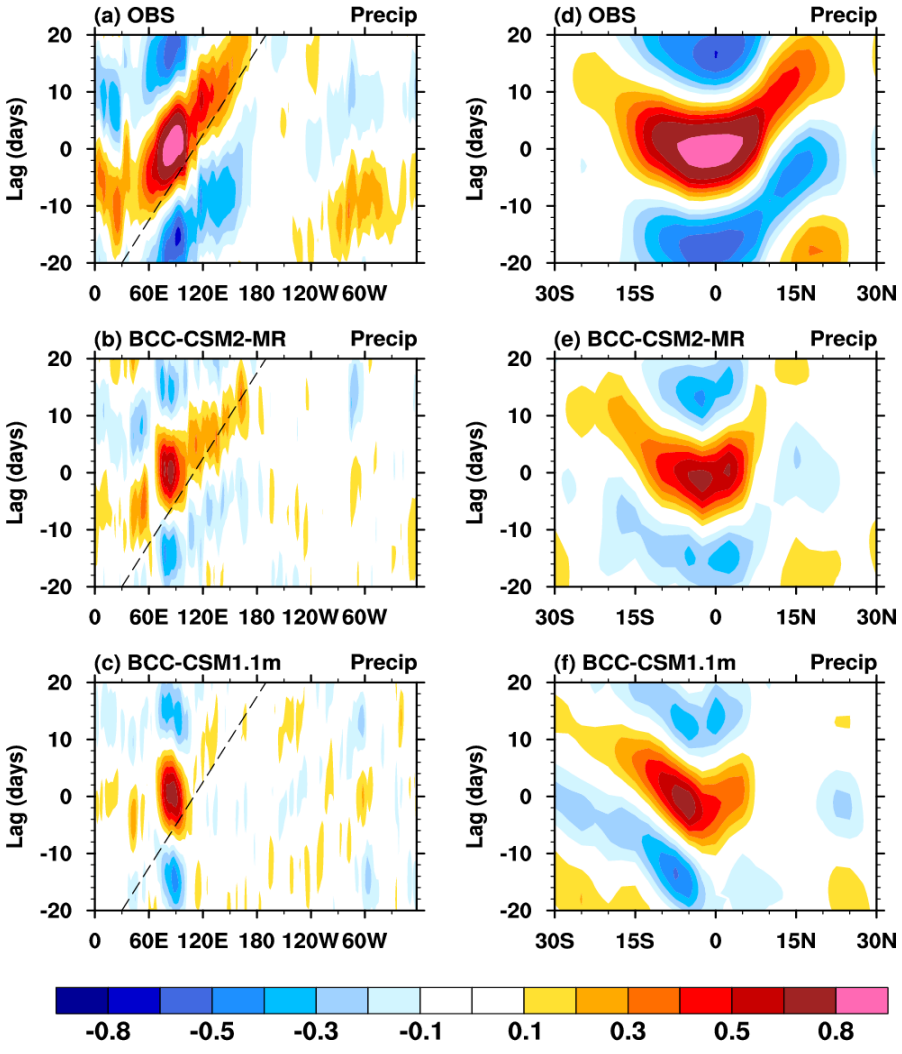

Figure 11. Left panels: longitude-time evolution of lagged correlation coefficient for the 20–100 day band-pass-filtered anomalous rainfall (averaged over 10 °S–10 °N) against itself averaged over the equatorial eastern Indian Ocean (75 °–85 °E; 5 °S–5 °N). Right panels: same as in the left panels but to show meridional propagation of the filtered rainfalls, and lagged correlation coefficient for anomalous rainfall (averaged over 80 °–100 °E) against the rainfall averaged over the same region of equatorial eastern Indian Ocean. Dashed lines in each panel denote the 5 m s^{-1} eastward propagation speed. The reference GPCP observations and historical simulations of models are from the period of 1997-2005.

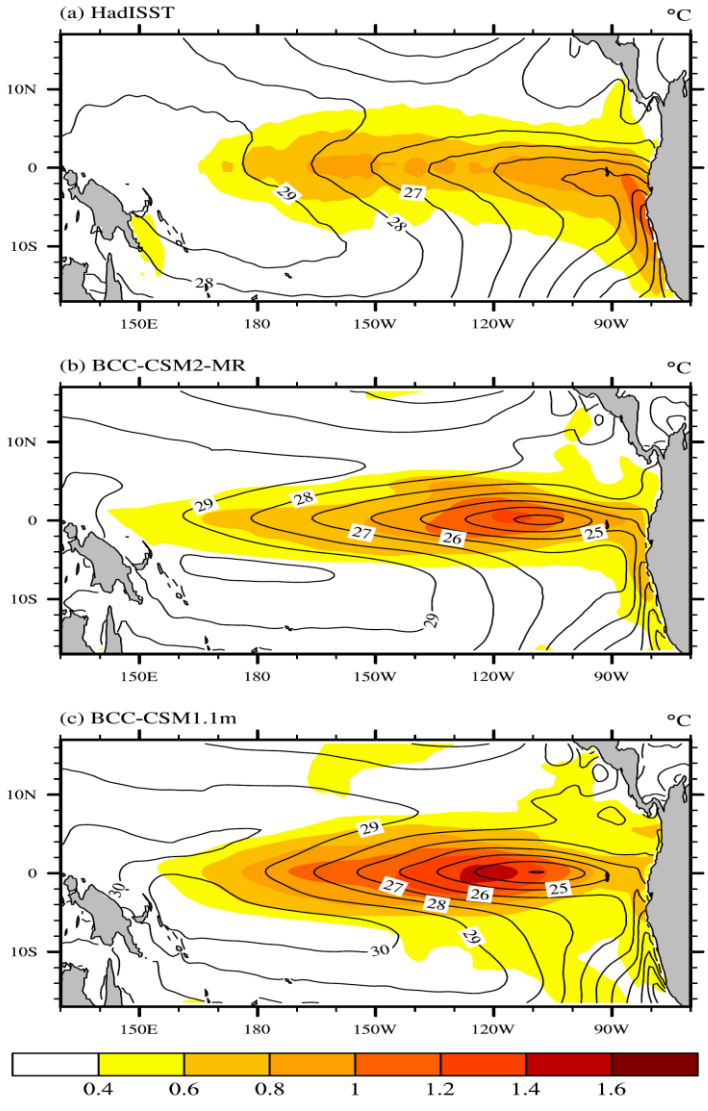

Figure 12. The spatial distributions of 1986-2005 annual mean sea surface temperature (contour lines, ℃) and its standard deviation of interannual anomalies (shaded area, ℃) in the tropical Pacific for (a) HadISST observations (Rayner et al., 2003), (b) BCC-CSM2-MR, (c) BCC-CSM1.1m.

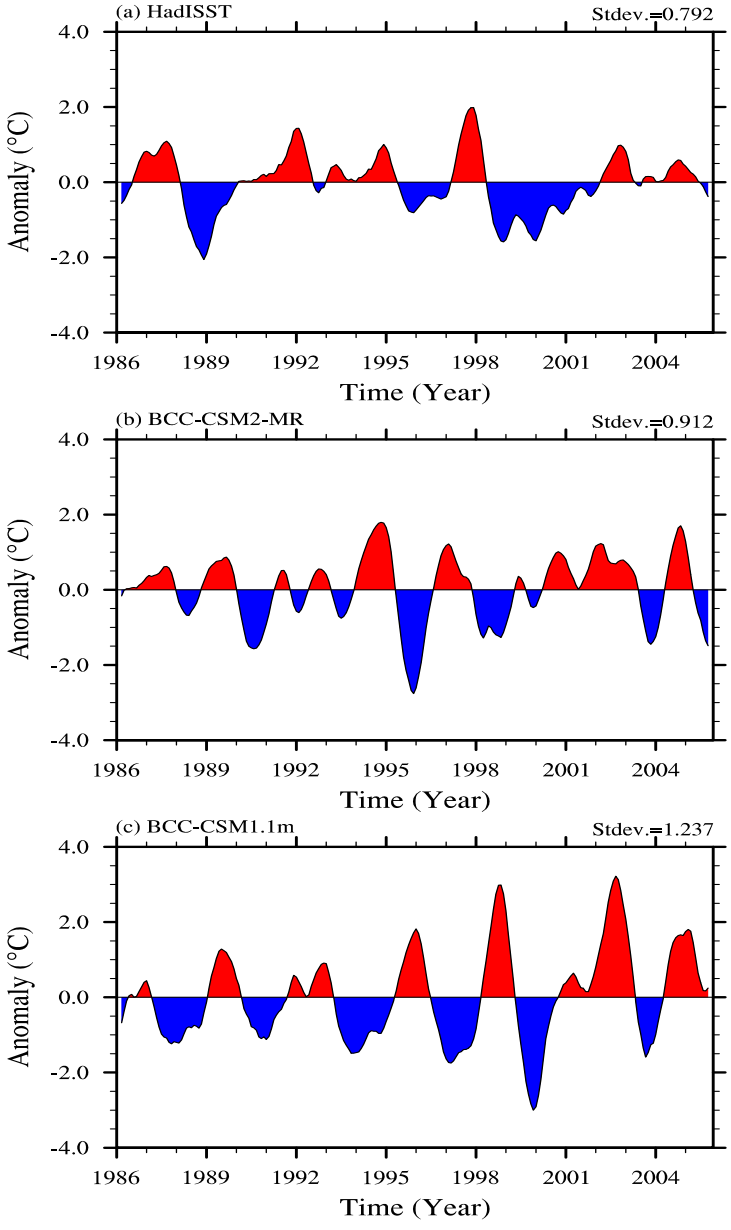

Figure 13. The time series of Nino3.4 SST Index from 1986 to 2005 for (a) HadISST data, (b) BCC-CSM2-MR, (c) BCC-CSM1.1m.

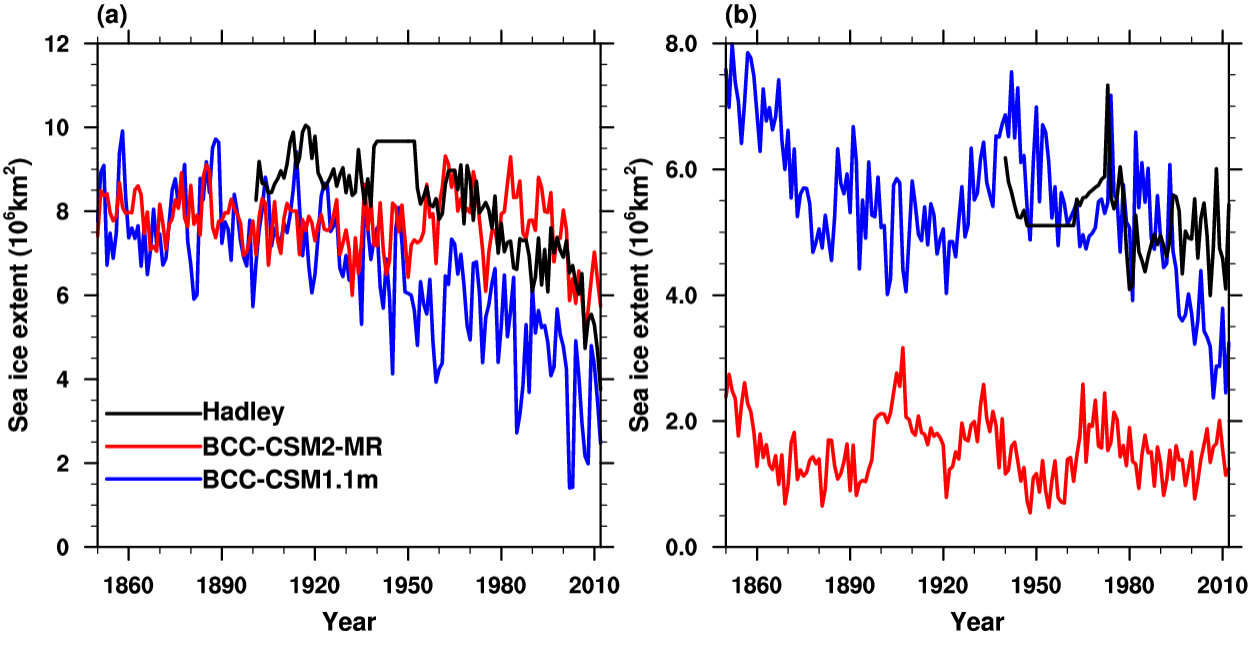

Figure 14. Time-series of sea-ice extent from 1851 to 2012 for (a) the Arctic in September and (b) the Antarctic in March as simulated in BCC-CSM2-MR and BCC-CSM1.1m and observations that are derived from Hadley Centre Sea Ice and Sea Surface Temperature data set (Rayner et al., 2003).

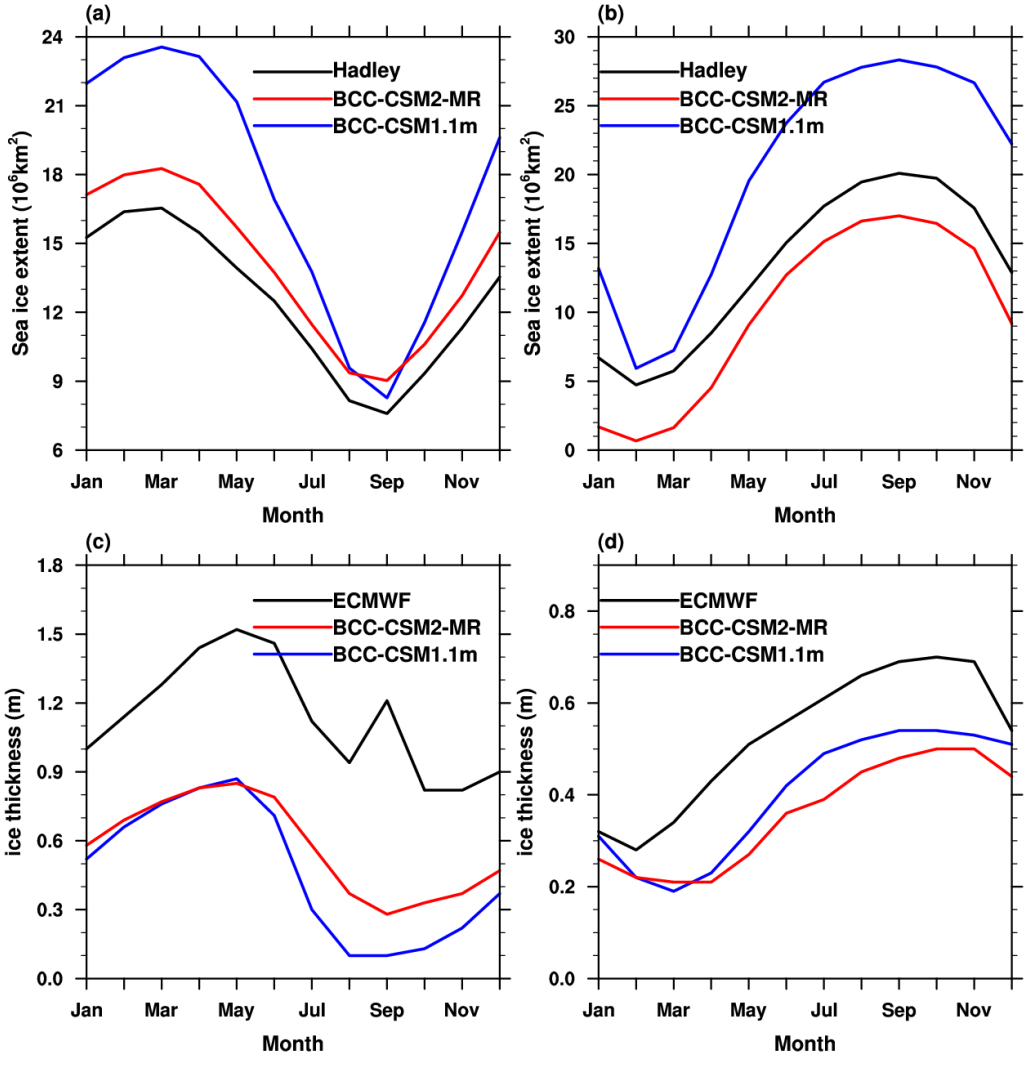

Figure 15. Mean (1980–2005) seasonal cycle of sea-ice extent (upper panel, the ocean area with a sea-ice concentration of at least 15%) and mean thickness (lower panel) in the Northern Hemisphere (left) and the Southern Hemisphere (right). The observed seasonal cycles of sea-ice extent in (a) and (b) are derived from 1980-2005 Hadley Centre Sea Ice and Sea Surface Temperature data set (Rayner et al., 2003), and the ice thickness in (c) and (d) are derived from 1980-2005 global gridded data set based on European Center for Medium-Range Weather Forecast (Tietsche, et al., 2014).

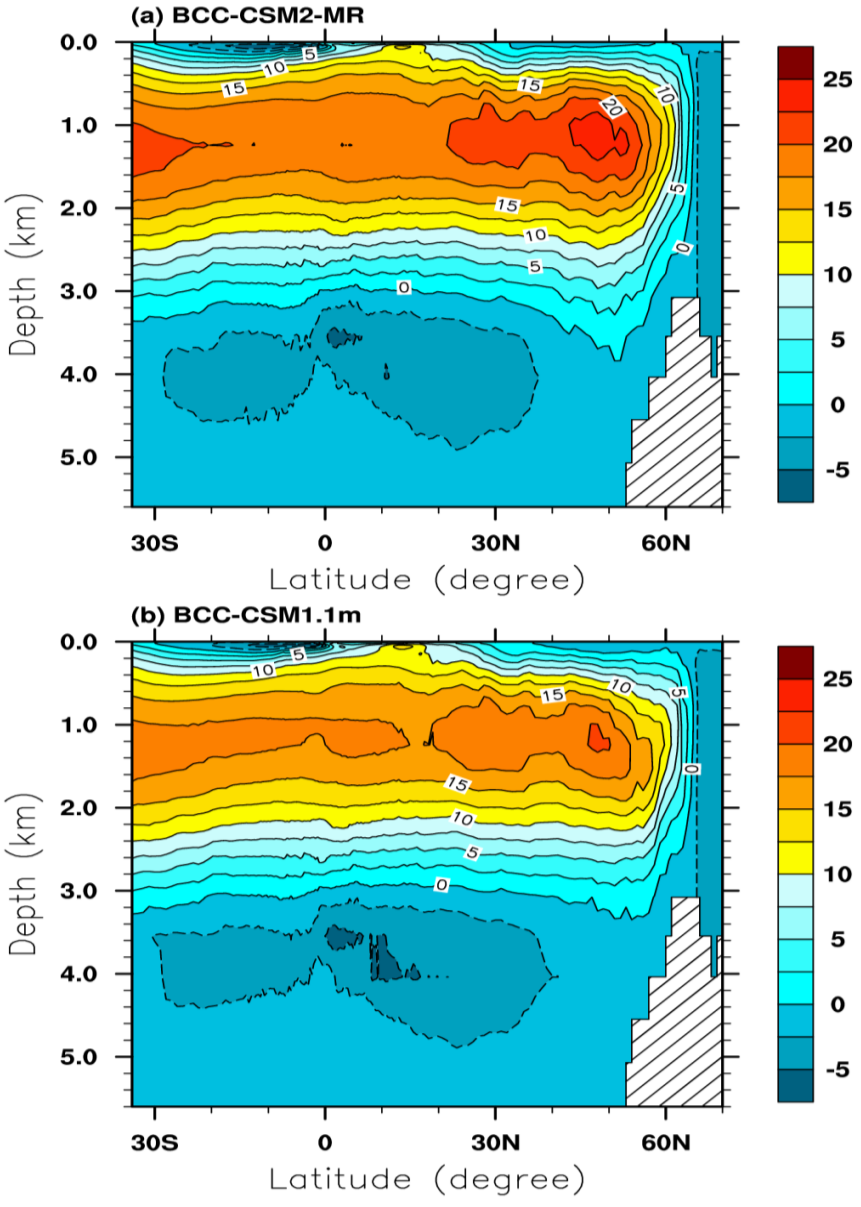

Figure 16. Zonally-averaged streamfunction of the Atlantic Meridional Overturning Circulation (AMOC) for the period of 1980 to 2005 in BCC-CSM2-MR (top) and BCC-CSM1.1m (bottom). Units: Sv

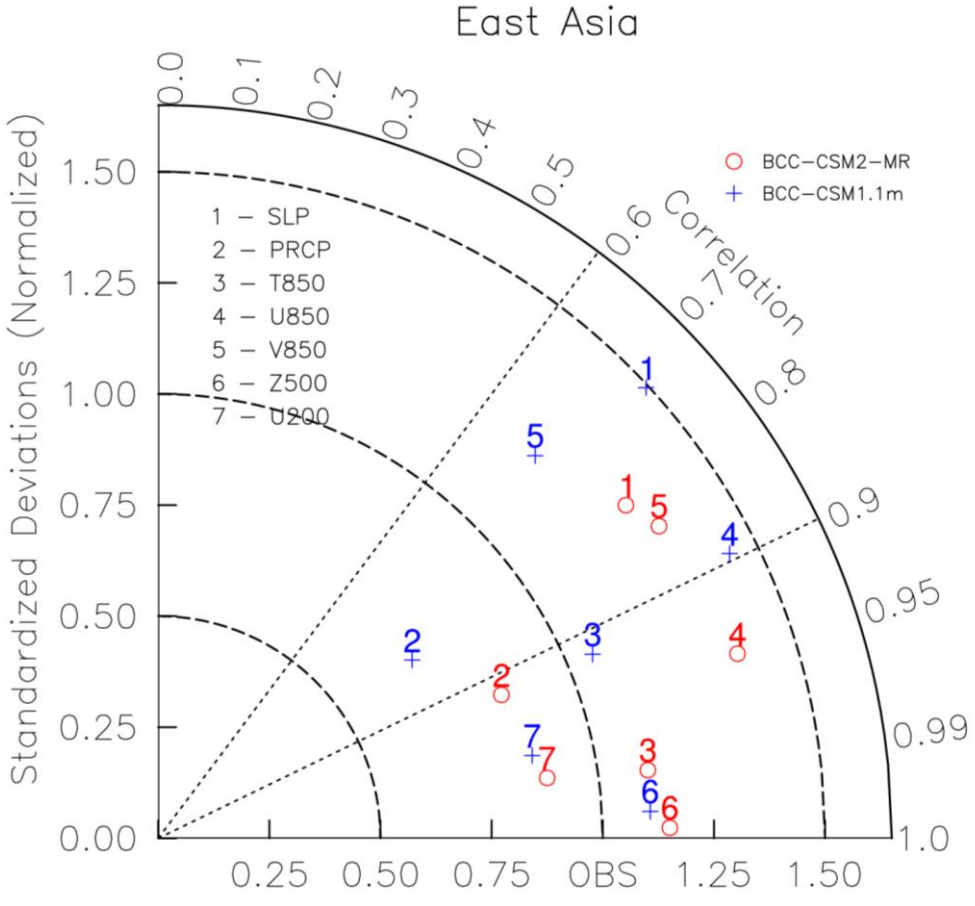

Figure 17. Same as in Figure 8, but for the domain covering East Asia (20°-50°N, 100°-140°E).

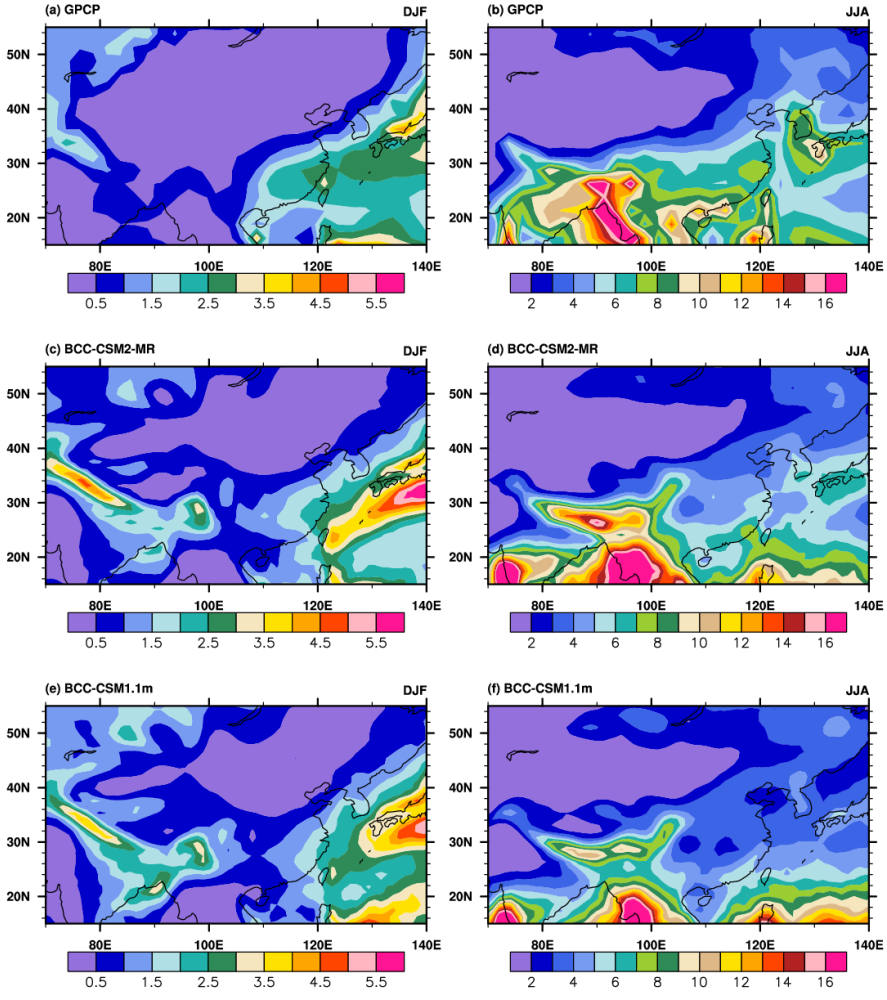

Figure 18. Regional distribution maps of precipitation climatology (averaged from 1980 to 2005) for December-January-February (left panels) and June-July-August (right panels) from (a) GPCP, (b) BCC-CSM2-MR, (c) BCC-CSM1.1m.

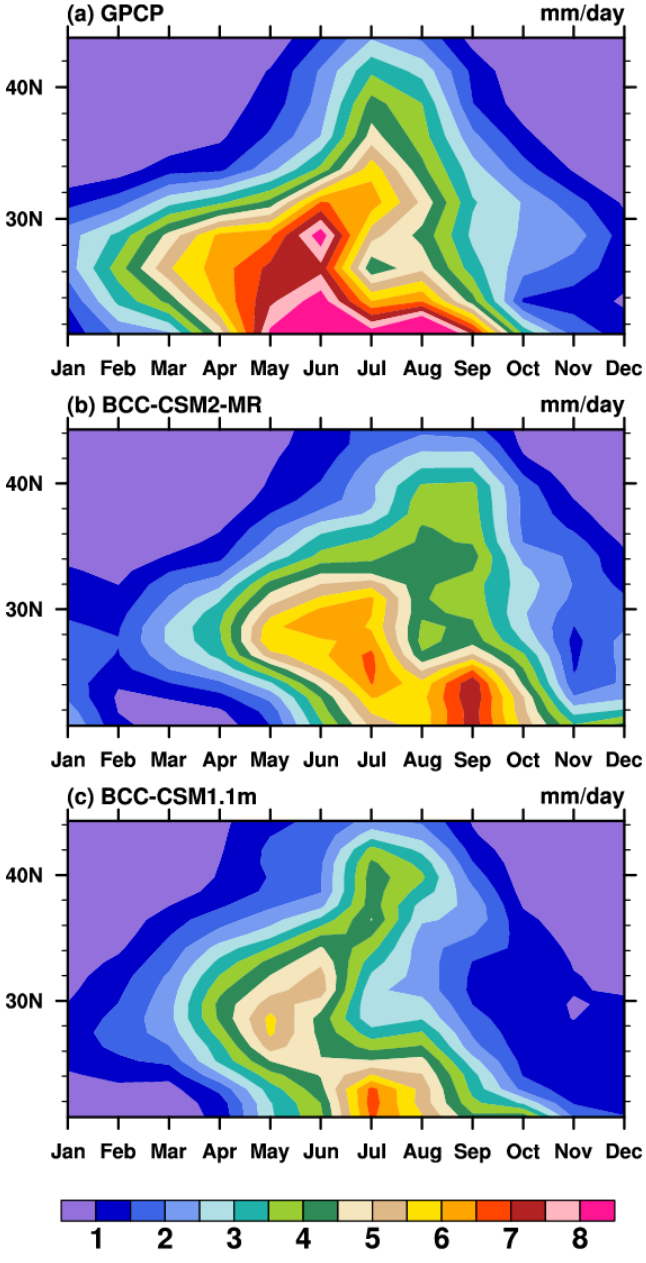

Figure 19. Latitude (from 20 ℃N to 25 ℃N) – month (Jan. to Dec.) diagrams showing variations of monthly precipitation averaged over 100 °-120 ℃E and for the period of 1980-2005. (a) GPCP, (b) BCC-CSM2-MR, (c) BCC-CSM1.1m.

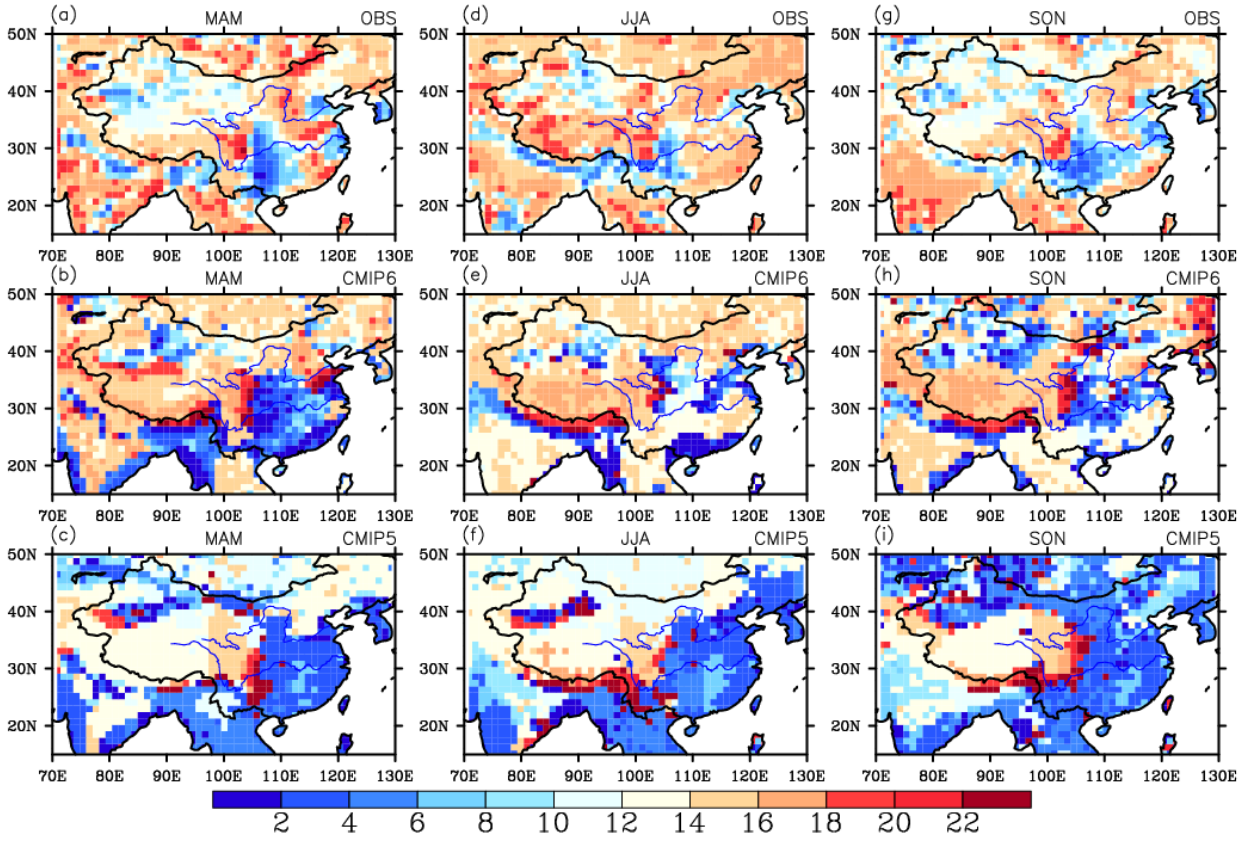

Figure 20. Local times of maximum frequency of rainfall occurrence in March-April-May (left column), June-July-August (middle column), and September-October-November (right column) over China and its surrounding areas for BCC-CSM2-MR (middle panel), BCC-CSM1.1m (bottom panel), and TRMM data (top panel, Huffman et al., 2014). The rainfall occurrence is defined as the hourly precipitation larger than 1 mm.